Contrib Mineral Petrol (1989) 102:429–453

Contributions to Mineralogy and Petrology

Magma mixing in the San Francisco Volcanic Field, AZ

Petrogenesis of the O'Leary Peak and Strawberry Crater Volcanics

Anne L. Bloomfield and Richard J. Arculus
Department of Geological Sciences, University of Michigan, Ann Arbor, MI 48109, USA

Abstract. A wide variety of rock types are present in the O'Leary Peak and Strawberry Crater volcanics of the Pliocene to Recent San Francisco Volcanic Field (SFVF), AZ. The O'Leary Peak flows range from andesite to rhyolite (56–72 wt % SiO_2) and the Strawberry Crater flows range from basalt to dacite (49–64 wt % SiO_2). Our interpretation of the chemical data is that both magma mixing and crustal melting are important in the genesis of the intermediate composition lavas of both suites. Observed chemical variations in major and trace elements can be modeled as binary mixtures between a crustal melt similar to the O'Leary dome rhyolite and two different mafic end-members. The mafic end-member of the Strawberry suite may be a primary mantle-derived melt. Similar basalts have also been erupted from many other vents in the SFVF. In the O'Leary Peak suite, the mafic end-member is an evolved (low Mg/(Mg+Fe)) basalt that is chemically distinct from the Strawberry Crater and other vent basalts as it is richer in total Fe, TiO_2, Al_2O_3, MnO, Na_2O, K_2O, and Zr and poorer in MgO, CaO, P_2O_5, Ni, Sc, Cr, and V. The derivative basalt probably results from fractional crystallization of the more primitive, vent basalt type of magma. This evolved basalt occurs as xenolithic (but originally magmatic) inclusions in the O'Leary domes and andesite porphyry flow. The most mafic xenolith may represent melt that mixed with the O'Leary dome rhyolite resulting in andesite preserved as other xenoliths, a pyroclastic unit (Qoap), porphyry flow (Qoaf) and dacite (Darton Dome) magmas. Thermal constraints on the capacity of a melt to assimilate (and melt) a volume of solid material require that melt mixing and not assimilation has produced the observed intermediate lavas at both Strawberry Crater and O'Leary Peak. Textures, petrography, and mineral chemistry support the magma mixing model. Some of the inclusions have quenched rims where in contact with the host. The intermediate rocks, including the andesite xenoliths, contain xenocrysts of quartz, olivine and oligoclase, together with reversely zoned plagioclase and pyroxene phenocrysts. The abundance of intermediate volcanic rocks in the SFVF, as observed in detail at O'Leary Peak and Strawberry Crater, is due in part to crustal recycling, the result of basalt-driven crustal melting and the subsequent mixing of the silicic melts with basalts and derivative magmas.

Offprint requests to: A.L. Bloomfield

Introduction

The San Francisco Volcanic Field (SFVF) is located on the southwestern edge of the Colorado Plateau close to the transition zone between the Colorado Plateau and the Basin and Range Province (Fig. 1). The volcanic rocks cap Mesozoic to PreCambrian sedimentary and metamorphic sequences which are exposed in the Oak Creek Canyon to the south and the Grand Canyon to the north. Volcanic activity in the SFVF began about 5 Ma ago (Damon et al. 1974) with the most recent eruption in 1064 AD (Smiley 1958). The SFVF extends over an area of roughly 5000 km^2 and is composed of six large silicic centers, which rise to a height of 3800 m, or about 1800 m above the general elevation of the Colorado Plateau in the region, and over 500 smaller basaltic and andesitic vents. Previous studies have shown that the SFVF contains an unusual volumetric abundance of calc-alkalic, intermediate composition lavas compared with Basin and Range Province magmatism of similar age (Robinson 1913; Wenrich-Verbeek 1979; Moore et al. 1974) and is in contrast with the primarily bimodal basalt and rhyolite magmatism typical of other post Oligocene volcanism in the southwestern U.S. (Christiansen and Lipman 1972).

The relative abundance of intermediate, calc-alkalic lavas cannot be explained by contemporaneous subduction

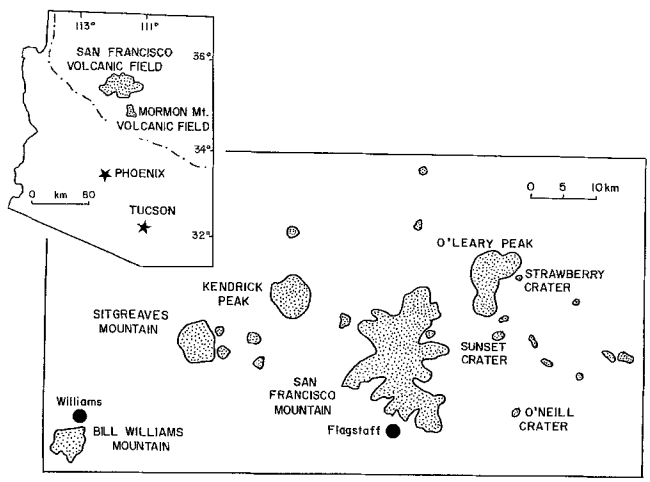

Fig. 1. Sketch map of the location of the San Francisco Volcanic Field in Arizona, with the main silicic centers shown in the stippled areas

of lithosphere beneath the Colorado Plateau. Projections of the evolution of the East Pacific Rise-San Andreas transform system (Dickinson and Snyder 1979) show that the last remnants of the subducted Farallon plate should have passed beneath the SFVF at least 10 Ma ago, 5 Ma prior to the onset of volcanism. A review by Gill (1981) of the time gap between cessation of subduction and associated magmatism suggests that these events are esssentially simultaneous, and are not generally charaterized by the inception and continuation of magmatism after a time interval of 5–10 Ma.

The abundance of anorogenic intermediate lavas in the SFVF has implications for our understanding of basalt-continental crust interactions and the chemical evolution of pre-existing crust by mobilization of low-melting point components. Many of the relative trace element abundances of the intermediate and silicic volcanics of the SFVF are similar to those of subduction-related magmas, yet appear to be inherited from crustal melting processes (Gust and Arculus 1986; Arculus 1987).

Basalt-driven crustal melting appears to be the primary process involved in the genesis of large silicic centers such as those of Yellowstone and Long Valley (Hildreth 1981). Although small in size relative to these centers, the SFVF is of particular interest because most, if not all, of the potential petrogenetic end-member components are exposed at the surface. These consist of mantle-derived basalts, mafic and ultramafic cumulate xenoliths (Stoeser 1974), lower crustal granulite xenoliths displaying partial melt features (Pushkar and Stoeser 1987), and rhyolitic and andesitic volcanic rocks. Many of the processes which can be readily sampled and deciphered in the SFVF may be representative of those which occur at much larger silicic systems.

Previous studies

A number of previous petrologic and isotopic studies of the SFVF have concentrated on the field as a whole and not on individual suites of cogenetic lavas. Even with these broad-based approaches, some features appear to be at odds with the geochemical trends expected as a result of magmatic evolution dominated by fractional crystallization. For example, rocks from the SFVF straddle the alkalic-subalkalic divisors of Irvine and Baragar (1971), MacDonald and Katsura (1964) and Le Bas et al. (1986). Trace element data for basaltic rocks also project in fields that transgress tectonic discriminant boundaries (Arculus 1987).

Previous workers have attributed the chemical variations in the SFVF to a variety of processes including fractional crystallization, melting of heterogeneous mantle and assimilation. Moore et al. (1974) studied the eastern and northern parts of the SFVF and recognized the gradational nature of the volcanics that span the gap between the Hawaiian alkalic trend of MacDonald (1968) and the Cascade

Table 1a. Chemical analyses of samples from O'Leary Peak

Sample	Xenoliths										
	72201A	72201B	72201D	72201F	72205B	72205C	72205D	72205E	73103B	73103C	73108B
SiO_2	49.76	50.42	53.47	55.97	53.18	53.45	54.74	53.38	57.56	55.52	54.53
TiO_2	2.58	2.45	2.18	1.87	2.29	2.17	2.00	2.18	1.92	1.91	2.00
Al_2O_3	17.18	16.96	16.80	16.28	17.07	17.43	17.27	17.10	15.85	16.39	16.89
Fe_2O_3	12.02	11.60	10.74	9.97	10.93	10.84	10.19	10.86	9.49	10.27	10.72
MnO	0.22	0.17	0.18	0.17	0.18	0.18	0.18	0.19	0.16	0.18	0.17
MgO	4.57	4.26	3.58	3.18	3.40	3.38	3.08	3.37	3.13	3.14	3.16
CaO	6.96	7.19	6.14	5.67	5.55	5.32	5.26	5.38	5.70	5.68	5.47
Na_2O	3.94	4.41	4.59	4.35	4.45	4.28	4.74	4.52	4.18	4.36	4.83
K_2O	2.22	1.62	1.88	2.04	2.24	2.29	2.34	2.36	1.50	1.81	2.01
P_2O_5	0.57	0.53	0.57	0.53	0.55	0.52	0.46	0.60	0.55	0.62	0.55
Total	100.03	99.62	100.13	100.02	99.85	99.86	100.25	99.95	100.04	99.88	100.32
Nb	39	32	34	32	36	38	38	38	34	33	33
Zr	309	249	314	311	299	316	299	327	278	336	348
Y	26	28	29	27	33	32	30	32	31	28	29
Sr	692	909	748	610	757	716	708	756	734	664	664
Th	1.7	–	2.4	1.6	0.8	3.2	3.1	3.2	2.3	0.8	3.2
Pb	4.9	5.4	5.7	7.0	8.8	17.0	10.5	10.3	5.8	4.5	4.6
Ga	18	19	17	18	18	18	19	20	16	19	19
Zn	79	68	69	80	130	143	139	139	63	76	78
Cu	–	–	–	3	5	9	8	4	–	–	1
Ni	5	3	–	5	–	2	–	1	2	2	1
U	–	–	–	1	–	–	–	1	–	–	–
Rb	43.8	14.3	21.8	20.2	30.7	33.7	36.9	34.6	16.0	17.2	22.3
Cr	–	–	–	–	–	–	–	–	–	–	–
Ce	73	73	76	75	76	78	80	84	72	75	74
Sc	12	17	14	12	16	14	16	13	11	13	10
Nd	30	21	25	31	26	40	33	27	33	38	33
Ba	644	629	707	681	727	780	792	692	692	726	698
V	142	112	81	71	76	68	54	58	72	75	74
La	38	41	35	25	42	56	50	38	36	35	37

Range trend of Carmichael (1964). The authors stressed that the history of the generation and evolution of the rock types is complex, and recognized no simple pattern of systematic magmatic evolution through time. Low $^{87}Sr/^{86}Sr$ ratios suggested to these authors that the lavas had experienced little (upper) crustal contamination. Evidence for fractional crystallization was presented in a study of mafic and ultramafic xenoliths from the SFVF by Stoeser (1974), who concluded that the xenoliths are cumulates resulting from differentiation of alkali olivine basalt intrusions emplaced in the crust at depths of up to 42 km (14 kbar). Wenrich-Verbeek (1979) studied a suite from Humphrey's Peak (one of the group forming San Francisco Mountain), and concluded that fractional crystallization had resulted in the formation of intermediate volcanics.

On the basis of distinctive Pb isotopic characteristics, Everson (1979) suggested that the generation of the different rock types (basalt through rhyolite) of the SFVF resulted from separate melting events of geochemically heterogeneous upper mantle source regions, established concurrently with the last major crustal formation event at about 1.6 Ga ago. Rapakivi feldspars in the O'Leary Peak rhyolite were studied by Bladh (1980), who concluded that these feldspars were the result of "basification" of the dome by the partial assimilation of xenolithic material. Tanaka et al. (1986) proposed that the magmatism in this anorogenic setting results from shear heating at the base of the lithosphere, and that the overall eastward drift of magmatism has resulted from absolute westward motion of the North American plate.

Purpose of study

It became apparent from a regional petrologic study (Arculus et al. in prep.), conducted as part of field-wide geologic investigations led by the United States Geological Survey, that unraveling of the petrogenetic processes would require detailed examination of individual eruptive centers. For example, a plot of MgO vs SiO_2 for samples from the SFVF analyzed by the U.S.G.S. (Moore and Wolfe 1987; Newhall et al. 1987; Ulrich and Bailey 1987; Wolfe et al. 1987a, b) illustrates the wide compositional variation within the SFVF as a whole (Fig. 2). It is difficult to ascribe observed chemical variations to particular petrogenetic processes with any confidence because there is no clear way to determine which samples are petrogenetically related. Consequently, two centers were chosen for detailed study: O'Leary Peak, which is one of the six large silicic centers, and Strawberry Crater, a small differentiated vent.

These two centers differ in total volume and general chemistry of erupted lavas. Strawberry Crater is considerably smaller than O'Leary Peak and is dominated by basalts and basaltic andesites whereas O'Leary Peak is dominated by dacites and rhyolites. These physical and geochemical

					Qord: northern dome					Qord: Darton Dome	
73110B	72201E	72902	72201C[a]	73103A	71902	72204	72205A	72905	72908	72909	72904
52.92	50.49	56.40	44.51	54.42	70.84	71.10	70.74	70.71	70.59	66.86	65.93
1.98	2.47	1.76	4.02	2.20	0.31	0.31	0.27	0.29	0.29	0.59	0.73
17.03	17.12	16.86	16.97	16.70	14.82	15.17	15.02	15.12	15.04	16.20	15.96
10.99	11.85	9.09	14.79	10.55	3.42	3.21	2.98	3.05	3.10	4.57	5.06
0.17	0.18	0.16	0.15	0.17	0.10	0.09	0.09	0.09	0.09	0.11	0.12
3.43	4.10	2.98	6.91	3.54	0.04	0.36	0.00	0.03	0.01	0.92	1.00
6.13	7.33	5.39	10.04	6.13	1.40	1.51	1.49	1.55	1.54	2.40	2.78
4.21	4.13	4.73	3.27	4.41	4.95	5.06	4.93	4.90	4.96	4.97	4.40
1.91	1.46	2.12	0.73	1.49	4.01	3.78	3.79	3.83	3.77	3.58	3.67
0.57	0.57	0.53	0.25	0.53	0.12	0.12	0.09	0.13	0.12	0.18	0.26
99.34	99.70	100.02	101.65	100.13	100.02	100.71	99.40	99.68	99.50	100.40	99.89
32	33	37	20	34	42	38	37	35	37	40	39
351	295	312	146	293	263	234	238	229	244	298	291
25	30	30	24	30	23	23	20	22	21	25	26
657	863	732	885	761	242	279	273	283	275	381	422
–	0.6	6.0	–	0.8	15.6	13.8	12.4	13.6	13.0	12.5	9.8
5.7	5.4	6.2	1.7	4.6	17.2	14.6	11.5	14.0	13.7	14.6	11.5
20	19	18	19	16	16	19	18	19	17	18	18
86	66	61	59	72	49	39	39	42	37	50	54
4	–	–	3	–	–	–	–	–	–	–	–
3	1	–	5	–	–	–	–	–	1	–	–
–	–	–	–	–	6	4	1	4	3	3	2
16.1	15.8	26.2	5.2	16.7	65.6	59.0	58.3	58.8	59.3	49.6	46.3
–	–	–	–	–	–	–	–	–	–	–	–
71	71	87	31	82	80	86	71	97	79	85	81
12	14	14	32	14	3	2	1	3	1	4	4
24	29	38	20	30	19	18	12	22	24	23	19
710	587	825	252	674	1111	1180	1171	1136	1058	1164	1113
72	107	53	261	84	1	7	2	7	1	11	19
36	33	48	2	34	56	57	48	63	43	58	60

Table 1a (continued)

Sample	Qord: Darton Dome	Qoaf					Qoap		Qorr	Qov and Qorv	
	72903	73106	73107	80305	73102	80301	72203A	72203G	72401	73009	72802
SiO_2	65.70	66.36	67.00	61.22	62.98	64.87	56.51	58.63	71.56	66.77	66.95
TiO_2	0.74	0.75	0.66	1.25	1.08	0.93	1.79	1.56	0.12	0.45	0.47
Al_2O_3	15.97	15.57	15.95	16.20	16.16	15.87	16.80	16.39	14.73	16.43	16.25
Fe_2O_3	5.10	5.03	4.72	7.10	6.48	5.83	9.16	8.27	2.57	4.68	4.62
MnO	0.11	0.11	0.11	0.14	0.13	0.12	0.16	0.15	0.10	0.15	0.14
MgO	1.22	1.19	1.00	2.13	1.76	1.48	2.92	2.51	0.09	0.35	0.39
CaO	3.13	2.63	2.44	4.16	3.56	3.32	5.57	4.99	1.01	2.40	2.46
Na_2O	4.78	4.98	4.74	4.65	4.91	4.97	4.94	4.78	5.26	5.63	5.28
K_2O	3.38	3.43	3.48	2.81	2.90	3.04	1.98	2.31	4.17	2.93	2.88
P_2O_5	0.23	0.19	0.23	0.39	0.32	0.27	0.53	0.48	0.03	0.17	0.17
Total	100.37	100.25	100.33	100.06	100.26	100.70	100.37	100.06	99.62	99.95	99.61
Nb	39	37	38	38	38	38	38	38	41	34	34
Zr	304	285	290	317	307	292	321	318	269	444	404
Y	26	24	26	27	27	25	30	29	29	26	26
Sr	422	394	368	559	501	462	690	621	143	486	489
Th	12.4	11.6	12.0	6.8	10.5	7.7	5.0	4.8	11.6	5.3	5.9
Pb	11.2	11.8	12.8	9.7	8.5	11.1	5.8	4.9	22.4	12.5	11.7
Ga	18	16	18	17	17	17	17	18	18	19	18
Zn	51	50	53	57	58	53	64	65	82	76	73
Cu	–	–	–	–	–	–	–	–	–	–	–
Ni	–	–	1	1	–	–	–	–	1	–	–
U	2	1	1	1	–	1	–	1	2	–	1
Rb	49.0	50.2	46.9	39.0	40.3	46.2	26.6	33.7	68.4	43.7	45.8
Cr	–	–	–	–	–	–	–	–	–	–	–
Ce	89	78	89	87	87	78	85	87	108	93	92
Sc	7	5	3	10	7	4	14	11	2	4	7
Nd	26	14	28	27	23	22	26	29	27	21	26
Ba	1074	1113	1149	924	975	991	766	807	1506	1304	1264
V	21	22	19	35	33	18	70	50	1	–	–
La	55	50	50	50	43	42	42	42	65	48	52

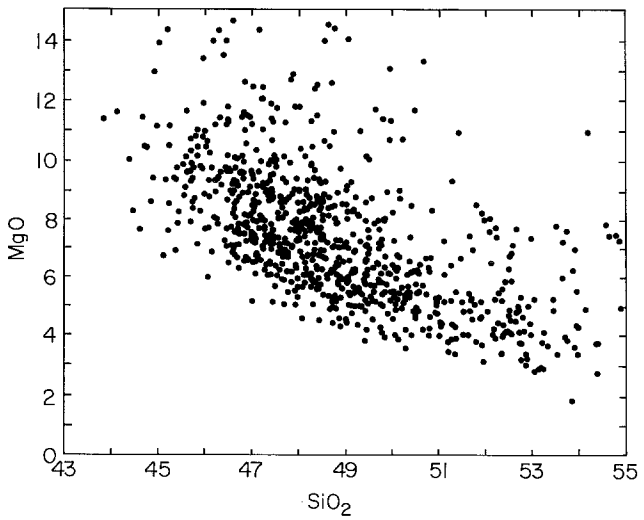

Fig. 2. MgO wt % vs SiO_2 wt % for samples collected throughout the SFVF by the USGS, data from Moore and Wolfe (1987), Newhall et al. (1987), Ulrich and Bailey (1987), Wolfe et al. (1987a), Wolfe et al. (1987b)

differences may reflect different processes involved in the evolution of the volcanic centers. However, the Strawberry and O'Leary centers may be fundamentally similar systems at different stages of evolution. A detailed geochemical study of these two centers provides insight into the processes involved in the evolution of these systems and may help us to understand the genesis of other SFVF suites and more generally, the formation of calc-alkaline andesites in an intracontinental, non-subduction zone setting.

Analytical techniques

Bulk chemistry

Whole rock bulk analyses were obtained using the University of Michigan Philips PW1400 Automated X-Ray Fluorescence Spectrometer equipped with a Rh target X-ray tube. Major element chemistry was measured on fused disks prepared from a mixture of whole rock powder and Li-tetraborate flux (Spectroflux 105), using methods similar to those of Norrish and Hutton (1969) and Harvey et al. (1973). Concentrations of 19 trace elements (Nb, Zr, Y, Sr, Th, Pb, Ga, Zn, Cu, Ni, U, Rb, Cr, Ce, Sc, Nd, Ba, V, La) were measured on pressed powder pellets using modifications of methods outlined by Norrish and Chappell (1967). Relative precision reported is generally $\pm 2\%$ for Rb and Sr; $\pm 3\%$ for Nb, Y, Pb, Sc, Ga, Zn and V; $\pm 5\%$ for Ba, Zr, Ni, Cr and Cu; and $\pm 10\%$ for La, Ce, Nd, Th and U. Where possible, fragments of xenolithic material, which are readily distinguished from host rocks on the basis of color, were hand picked and removed from the rock fragments to be analyzed. Major and trace element chemistry for the samples analyzed are displayed in Table 1 and CIPW normative mineralogies are presented in Table 2.

				Qoo and Qoov							Qod
72801	72808	73114	72809	73007	73011	73004	73006	72006	73005	72001	73001
67.84	66.46	67.36	67.14	69.38	71.58	67.35	68.79	67.68	67.96	67.65	66.92
0.41	0.44	0.35	0.43	0.23	0.16	0.35	0.26	0.32	0.32	0.34	0.44
16.02	16.09	15.78	16.33	15.42	14.95	16.27	15.65	16.17	15.89	15.81	16.07
4.72	4.63	4.48	4.67	3.53	2.83	4.61	3.82	4.37	4.40	4.42	4.46
0.14	0.14	0.15	0.14	0.11	0.10	0.16	0.12	0.14	0.14	0.14	0.13
0.27	0.64	0.69	0.60	0.40	0.30	0.51	0.49	0.46	0.56	0.88	0.67
2.15	2.74	2.48	2.37	1.91	1.55	2.18	1.83	2.04	2.15	2.16	2.34
5.40	5.34	5.51	5.53	5.46	4.97	5.76	5.49	5.33	5.74	5.60	5.46
2.91	2.95	3.04	2.90	3.51	4.14	3.06	3.48	3.29	3.06	2.98	2.96
0.23	0.33	0.14	0.16	0.16	0.05	0.13	0.11	0.15	0.15	0.12	0.18
100.08	99.75	99.98	100.27	100.11	100.64	100.37	100.03	99.95	100.36	100.10	99.63
34	33	34	34	37	40	35	35	35	35	33	34
533	450	559	467	420	309	582	473	547	546	553	389
25	26	26	27	27	29	27	29	30	26	28	26
441	485	426	479	289	185	420	324	403	394	418	467
7.0	4.7	6.4	7.1	10.0	10.3	7.0	7.3	4.1	7.5	4.1	8.7
9.1	12.9	12.1	14.0	11.9	15.4	9.4	12.7	12.7	13.8	11.6	13.1
20	18	18	19	19	18	18	18	19	19	19	18
81	79	75	76	64	75	69	105	75	74	75	69
–	–	–	–	–	–	–	–	–	–	–	–
1	–	–	–	–	–	4	3	1	–	–	–
–	–	1	–	2	1	3	1	1	–	3	1
44.7	43.8	45.7	44.8	54.1	63.7	42.3	55.9	46.4	40.6	46.4	46.6
–	–	–	–	–	–	–	–	–	–	–	–
92	83	92	96	98	102	103	99	101	95	92	90
3	3	3	3	0	0	5	1	3	2	3	3
27	22	26	25	21	26	32	23	23	23	24	25
1351	1323	1384	1317	1510	1493	1468	1551	1449	1463	1339	1227
2	–	–	–	–	–	1	5	1	–	5	–
52	51	50	60	58	62	61	57	57	56	47	52

Mineral chemistry

Mineral chemistry was determined using the University of Michigan Cameca Camebax electron microprobe, using 15 kV accelerating voltage and 10 nA beam current. Peaks and backgrounds were counted for 30 s. For feldspar analyses, the electron beam was rastered over a six micron area to reduce Na volatilization. Representative mineral analyses are presented in Tables 3–7. Feldspar and pyroxene compositions are plotted in Figs. 3 and 4.

O'Leary Peak and Strawberry Crater – General description

The O'Leary Peak suite, as mapped by Moore and Wolfe (1976), is composed of seven major volcanic units extending over an area of approximately 50 km^2 (Fig. 5). The highly silicic units form thick flows and topographically prominent domes. Numerous Pleistocene to Recent basaltic cinder cones and basalt flows are located in the vicinity of O'Leary Peak. The rhyolitic dome rises to 2725 m, some 700 m above the surrounding plateau. The dome has been dated by K–Ar methods as 233 ± 37 ka (Damon et al. 1974).

From oldest to youngest, the eruptive sequence determined from stratigraphic relationships by Moore et al. (1974) includes an andesite porphyry flow (Qoaf), the rhyolite porphyry domes of O'Leary Peak (Qord), a rhyodacite obsidian flow (Qoo), and the rhyodacite flow of Deadman Mesa (Qor). Other units, whose relative ages are less well constrained, include a poorly exposed dacite flow (Qod) that underlies Qoo; the rhyodacite dome of Robinson Crater (Qorr) that overlies Qoaf and Qord; and an andesite pyroclastic deposit (Qoap) that occurs on the flanks of the domes (Moore et al. 1974).

Strawberry Crater is located just east of the Deadman Mesa lava flow of O'Leary Peak and about 6 km northeast of O'Leary Peak dome (Fig. 5). Strawberry Crater is a differentiated vent composed of a series of pyroclastic deposits that form a cinder cone (Qmac), a small andesitic plug (Qmr), and a lava flow (Qma) that extends for about 4 km to the northeast. The units have been constrained with K–Ar methods to the last 100 ka (46 ± 46 ka) (Damon et al. 1974).

Classification and petrography

O'Leary Peak

The O'Leary lavas vary between 56 and 72 wt % SiO_2 (Table 1). There are also xenoliths with 49–58 wt % SiO_2 entrained in the O'Leary rhyolite domes and andesite porphyry flow. According to the classification proposed by Le Bas et al. (1986), the O'Leary Peak suite is generally alkaline, spanning the range from hawaiite (the most mafic xenoliths) through mugearite and benmoreite to trachyte and alkali rhyolite (Fig. 6). However, the modal and normative mineralogies of the samples are more typical of a subalkaline suite. All O'Leary samples are silica-saturated (with the exception of one xenolith with minor normative nepheline) and have normative hypersthene. In addition, most samples contain normative quartz and many contain normative corundum. This is consistent with the observed modal mineralogy: groundmass hypersthene is common, as is quartz in the more silicic samples. Furthermore,

Table 1b. Chemical analyses of Samples from Strawberry Crater and other basaltic vents

Sample	Vents							Strawberry Crater	
	81001	81003	81002	81004	80404	80405	73105A	Qmac 80302G	Qmac 80302A
SiO_2	49.91	48.33	49.68	49.37	47.12	47.06	47.29	49.15	55.63
TiO_2	1.33	1.42	1.34	1.21	1.41	1.40	1.62	1.33	1.04
Al_2O_3	14.81	17.18	14.76	15.54	12.69	12.59	15.23	15.41	15.27
Fe_2O_3	10.02	10.81	10.13	10.28	10.68	10.70	11.95	10.72	8.17
MnO	0.16	0.18	0.17	0.17	0.17	0.18	0.17	0.17	0.14
MgO	8.25	6.73	8.30	8.26	12.89	12.96	8.79	8.14	5.40
CaO	10.31	9.89	10.50	10.36	10.82	10.87	10.14	10.27	7.73
Na_2O	2.98	3.18	2.90	2.81	2.18	2.17	3.12	2.90	3.70
K_2O	1.13	0.84	1.09	0.91	0.72	0.67	0.82	0.95	2.08
P_2O_5	0.61	0.86	0.62	0.74	0.60	0.57	0.51	0.64	0.47
Total	99.52	99.41	99.50	99.64	99.28	99.16	99.65	99.70	99.63
Nb	42	42	41	40	34	35	27	42	35
Zr	216	219	205	202	173	169	179	205	266
Y	20	24	20	21	18	18	24	21	18
Sr	774	954	774	779	668	674	605	785	619
Th	14.5	15.6	13.8	15.4	8.3	8.3	1.7	11.5	14.8
Pb	5.2	1.6	4.7	3.1	3.2	0.5	1.1	6.9	3.8
Ga	17	21	18	17	15	16	18	19	17
Zn	67	71	67	68	66	63	78	75	59
Cu	85	30	110	58	51	51	80	16	46
Ni	85	35	91	77	265	261	152	83	45
U	–	–	2	1	–	–	–	–	1
Rb	11.4	6.6	10.6	9.8	5.8	6.6	12.1	10.8	17.8
Cr	246	32	237	121	967	995	397	241	106
Ce	142	148	132	140	83	81	69	143	122
Sc	30	31	30	29	34	34	33	30	21
Nd	38	45	38	46	30	32	30	42	35
Ba	1083	1290	1049	1094	794	804	515	1023	1113
V	214	211	205	220	217	222	214	215	159
La	82	93	75	89	42	46	25	85	78

Table 2a. CIPW normative mineralogy of samples from O'Leary Peak[a]

	Xenoliths										
	72201A	72201B	72201D	72201F	72205B	72205C	72205D	72205E	73103B	73103C	73108B
Q	–	–	–	4.49	–	0.31	–	–	9.59	4.67	0.09
C	–	–	–	–	–	–	–	–	–	–	–
Or	12.95	9.38	11.94	12.91	14.16	14.74	14.87	14.84	9.50	11.55	12.86
Ab	32.59	36.65	41.60	39.35	40.27	39.40	43.25	40.70	37.80	39.81	44.41
An	22.27	21.35	21.10	20.21	21.37	23.52	20.39	20.64	21.43	21.31	20.04
Ne	0.17	–	–	–	–	–	–	–	–	–	–
Di	6.79	8.66	6.38	5.13	3.54	1.31	3.78	2.97	4.15	3.96	4.57
Hy	–	0.23	7.78	8.35	8.03	10.08	8.49	7.54	8.21	8.79	8.91
Ol	14.93	12.87	1.75	–	1.98	–	0.18	2.83	–	–	–
Mt	2.58	2.49	2.51	2.32	2.55	2.57	2.39	2.52	2.21	2.41	2.54
Il	4.84	4.58	4.45	3.82	4.67	4.50	4.10	4.42	3.91	3.92	4.13
Ap	1.25	1.16	1.33	1.26	1.30	1.24	1.08	1.41	1.30	1.46	1.32
Total	98.38	97.35	98.85	97.84	97.87	97.67	98.52	97.86	98.10	97.89	98.88

[a] Weight based norms using $FeO/(FeO+Fe_2O_3)=0.85$

in terms of the normative-type discriminants of Irvine and Baragar (1971), the O'Leary suite projects almost entirely within subalkaline fields (and specifically calc-alkaline) (Fig. 7).

A number of voluminous silicic ash flows, which appear to be subalkaline magmas on the basis of mineralogical characteristics, contain comparable but relatively high combined alkali contents (e.g., Carpenter Ridge ($\simeq$1500 km^3) with 8.1–9.2 (Na_2O+K_2O) wt % for lavas in the range of 66%–73% SiO_2 (Lipman 1975) and Rainier Mesa ($\simeq$1000 km^3) with 9.4–8.6 (Na_2O+K_2O) wt % in the range 69%–77% SiO_2 (Quilivan and Byers 1977).

Strawberry Crater								
Qmac 72206C	Qmac 80302E	Qmac 80302C	Qmac 72206A	Qma 80403	Qma 80402	Qma 80401	Qmr 80303	Qmr 80304
55.80	49.83	49.05	57.11	59.35	59.49	54.12	63.98	59.69
1.03	1.36	1.29	0.96	0.92	0.87	1.11	0.64	0.83
15.43	15.21	14.80	15.42	15.56	15.34	15.09	15.40	15.17
8.15	10.33	10.14	7.68	7.07	6.85	8.88	5.33	6.89
0.14	0.17	0.17	0.14	0.13	0.12	0.15	0.11	0.12
5.34	7.57	7.92	4.72	4.04	4.02	6.63	2.69	4.44
7.51	11.99	12.65	6.85	5.98	6.25	8.14	4.24	6.10
3.74	2.89	2.60	3.83	3.98	4.01	3.41	4.33	4.07
2.08	1.05	0.88	2.30	2.56	2.65	1.77	3.37	2.69
0.47	0.64	0.64	0.43	0.41	0.40	0.50	0.27	0.40
99.69	101.04	100.13	99.44	99.99	100.00	99.79	100.36	100.41
35	40	38	34	34	33	36	28	33
266	215	202	286	306	308	249	326	296
19	21	20	18	18	17	18	17	17
618	816	791	600	565	529	642	428	527
15.4	13.5	14.0	12.9	11.8	12.5	13.7	14.0	13.9
6.6	4.3	2.9	6.9	7.1	8.0	4.9	9.0	7.1
18	18	17	16	17	16	17	16	17
59	70	69	54	57	54	61	45	53
48	49	33	27	28	25	22	9	18
50	69	72	39	28	31	79	22	40
–	1	1	2	1	1	–	1	1
18.5	9.0	8.4	21.6	23.0	24.5	16.8	30.6	23.6
115	155	203	93	37	63	127	66	126
124	133	127	117	114	122	115	107	118
18	30	29	13	14	15	24	10	16
37	44	35	37	35	31	37	23	32
1100	1029	976	1181	1207	1223	1093	1240	1195
149	236	286	113	109	109	159	66	103
75	75	74	74	75	72	81	75	79

					Qord: northern dome					Qord: Darton Dome	
73110B	72201E	72902	73103A	72201C[b]	71902	72204	72205A	72905	72908	72909	72904
0.51	–	3.43	2.92	–	22.65	22.50	23.46	23.25	23.03	16.26	17.49
–	–	–	–	–	0.15	0.57	0.65	0.85	0.60	0.45	0.64
12.22	8.98	13.40	9.53	4.21	24.27	22.81	22.77	22.92	22.55	21.56	22.20
38.57	36.26	42.80	40.33	18.25	42.87	43.77	42.39	41.93	42.53	42.91	38.13
23.81	24.75	19.85	23.12	28.76	6.31	6.88	6.93	6.90	6.97	10.94	12.38
–	–	–	–	4.74	–	–	–	–	–	–	–
4.29	7.67	4.28	5.07	15.60	–	–	–	–	–	–	–
9.59	4.16	7.82	9.18	–	1.64	2.06	1.36	1.43	1.43	3.51	3.81
–	8.03	–	–	17.68	–	–	–	–	–	–	–
2.60	2.68	2.12	2.49	3.15	0.76	0.71	0.66	0.67	0.68	1.02	1.13
4.09	4.88	3.58	4.52	7.48	0.61	0.59	0.53	0.55	0.55	1.15	1.42
1.36	1.30	1.24	1.25	0.53	0.27	0.27	0.21	0.29	0.26	0.41	0.58
97.04	98.69	98.54	98.42	100.39	99.54	100.17	98.96	98.80	98.60	98.20	97.78

[b] cumulate

Clearly, classification based solely on alkali versus silica content can be somewhat inconsistent with mineralogical characteristics. In this account, units are referred to by their mapped name (subalkaline nomenclature), but the alkalic terms are also used in discussion of the geochemical variations observed.

Rhyolite domes (Qord). The rhyolite dome has been mapped as one unit, but there are actually two different domes with somewhat different chemistries: the northern dome and Darton Dome. The northern dome is an alkali rhyolite with 70.5%–71.1 wt % SiO_2, while Darton Dome is a quartz trachyte with 65.7–66.9 wt % SiO_2.

Table 2a (continued)

Sample	Qord: Darton Dome	Qoaf					Qoap		Qorr	Qor and Qorv	
	72903	73106	73107	80305	73102	80301	72203A	72203G	72401	73009	72802
Q	15.35	15.87	18.18	10.30	11.92	14.12	2.84	6.66	21.27	15.61	17.98
C	–	–	1.03	–	–	–	–	–	–	0.08	0.76
Or	20.46	20.94	21.07	17.54	17.96	18.73	12.58	14.56	24.44	17.84	17.61
Ab	41.40	43.61	41.19	41.52	43.50	43.79	44.91	43.15	44.14	49.09	46.20
An	12.41	10.36	10.87	15.86	14.16	12.51	19.10	17.53	4.23	11.14	11.51
Ne	–	–	–	–	–	–	–	–	–	–	–
Di	1.59	1.51	–	2.70	1.81	2.36	5.69	4.66	0.43	–	–
Hy	3.80	3.77	3.69	5.93	5.26	4.38	7.40	6.58	1.27	2.75	2.77
Ol	–	–	–	–	–	–	–	–	–	–	–
Mt	1.14	1.13	1.06	1.63	1.48	1.32	2.14	1.92	0.55	1.05	1.04
Il	1.45	1.47	1.29	2.51	2.15	1.85	3.67	6.17	0.23	0.89	0.92
Ap	0.52	0.44	0.53	0.90	0.73	0.61	1.26	1.12	0.06	0.38	0.38
Total	98.13	99.11	98.96	98.90	98.90	99.68	99.59	99.36	96.63	98.84	99.17

Table 2b. CIPW normative mineralogy of Strawberry Crater and other basaltic vents[a]

Sample	Vents							Strawberry Crater	
	81001	81002	81003	81004	80404	80405	73105A	Qmac 80302G	Qmac 72206C
Q	–	–	–	–	–	–	–	–	2.65
C	–	–	–	–	–	–	–	–	–
Or	6.64	6.41	5.00	5.50	4.05	3.75	4.62	5.65	13.14
Ab	25.00	24.52	27.18	24.28	17.49	17.47	22.21	24.63	33.84
An	23.45	23.97	30.47	27.75	21.60	21.49	24.01	26.28	20.46
Ne	–	–	–	–	–	–	1.63	–	–
Di	20.05	20.57	11.47	17.07	22.25	22.71	17.91	17.67	13.70
Hy	3.53	3.63	3.26	5.83	1.74	1.65	–	3.83	9.50
Ol	13.36	13.40	14.31	12.25	25.53	25.68	20.96	14.39	–
Mt	2.16	2.20	2.38	2.29	2.21	2.22	2.49	2.34	1.90
Il	2.51	2.55	2.73	2.35	2.55	2.53	2.94	2.55	2.10
Ap	1.33	1.37	1.90	1.67	1.26	1.20	1.06	1.42	1.10
Total	98.04	98.62	98.70	98.99	98.68	98.70	97.84	98.76	98.40

Sample	Strawberry Crater								
	Qmac 80302E	Qmac 80302C	Qmac 72206A	Qmac 80302A	Qma 80403	Qma 80402	Qma 80401	Qmr 80303	Qmr 80304
Q	–	–	4.80	2.42	7.77	7.43	0.79	12.77	6.72
C	–	–	–	–	–	–	–	–	–
Or	6.04	5.03	14.55	12.99	16.06	16.56	11.35	20.69	16.76
Ab	23.73	21.38	34.76	33.03	35.70	35.90	31.37	38.03	36.33
An	24.72	25.39	19.38	19.98	18.03	16.97	22.50	13.12	16.01
Ne	–	–	–	–	–	–	–	–	–
Di	24.88	27.09	11.97	14.75	9.03	11.12	15.35	5.83	11.28
Hy	0.26	0.66	8.71	9.18	7.85	7.19	11.96	5.45	7.88
Ol	14.47	13.80	–	–	–	–	–	–	–
Mt	2.19	2.15	1.79	1.88	1.63	1.58	2.11	1.21	1.59
Il	2.52	2.39	1.97	2.08	1.85	1.75	2.31	1.27	1.68
Ap	1.37	1.37	1.01	1.09	0.95	0.93	1.20	0.62	0.92
Total	100.16	99.27	98.94	97.39	98.87	99.41	98.94	99.00	99.17

[a] Weight based norms using $FeO/(FeO+Fe_2O_3)=0.85$

				Qoo and Qoov							Qod
72801	72808	73114	72809	73007	73011	73004	73006	72006	73005	72001	73001
18.70	16.24	16.03	16.48	18.70	21.61	15.08	17.57	17.27	16.13	16.37	16.60
1.30	–	–	0.35	–	–	–	–	0.99	–	–	0.12
17.46	17.86	18.30	17.79	21.23	24.24	18.64	20.96	19.70	18.58	18.26	18.18
46.38	46.31	47.52	48.62	47.31	41.66	50.27	47.41	45.70	79.90	49.16	47.96
9.29	11.56	9.56	11.13	7.35	6.19	9.80	7.97	9.23	8.81	9.51	10.87
–	–	–	–	–	–	–	–	–	–	–	–
–	0.14	1.68	–	1.01	0.90	0.42	0.48	–	0.92	0.63	–
2.62	3.17	2.85	3.20	2.10	1.60	2.95	5.52	2.80	2.81	3.46	3.20
–	–	–	–	–	–	–	–	–	–	–	–
1.05	1.03	1.00	1.06	0.79	0.61	1.04	0.85	0.97	0.98	1.00	1.01
0.79	0.85	0.68	0.85	0.46	0.30	0.69	0.51	0.62	0.62	0.66	0.87
0.51	0.75	0.32	0.36	0.37	0.11	0.29	0.24	0.34	0.34	0.28	0.40
98.09	97.91	97.92	99.85	99.31	97.23	99.19	98.50	97.62	99.10	99.33	99.22

The domes contain abundant large phenocrysts of plagioclase (up to 1.5 cm), quartz, sanidine (commonly mantled by plagioclase) and partially altered amphibole, in a light gray to brown groundmass composed of similar minerals and hematite (probably a subsolidus oxidation product). The feldspars display a range of compositions, including partially melted andesine feldspars that appear to be in disequilibrium with the bulk rock compositions (Figs. 3 and 8f) and reversely zoned feldspar phenocrysts with An_{15} cores, An_{23} midway between the core and rim, and An_{17} rims. The domes contain abundant basaltic and andesitic xenoliths that are described below.

Andesite porphyry flow (Qoaf). Samples of the andesite porphyry flow exhibit a wide range of compositions, from 61–67 wt % SiO_2 (benmoreite to trachyte). Samples contain phenocrysts of plagioclase, altered amphibole, clinopyroxene and orthopyroxene (commonly reversely zoned), and biotite in a fine grained groundmass with similar mineralogy. Numerous disequilibrium textures are evident in thin section, including olivine xenocrysts with pyroxene reaction rims; quartz xenocrysts with pyroxene and glass reaction rims; corroded Mg-rich, clinopyroxene phenocrysts with compositions that are not in equilibrium with orthopyroxene phenocrysts (cf., Huebner and Turnock 1980; Fig. 4); abundant feldspars with corroded "sieve" textures (Fig. 8e, f) and large (0.5 cm) sanidine phenocrysts (xenocrysts?) with plagioclase mantles. Sample 73106 contains orthopyroxene with reverse zoning from Mg No. = 100 Mg/[Mg + Fe^{2+}] = 40 in the core to 59 in the rim. Clinopyroxene in the sample is less prominently zoned with Mg No. = 40 in the core to 42 in the rim.

Xenoliths identical to those found in Qord are also found in Qoaf. Many samples contain small xenoliths (1 cm in diameter) and small xenocrystic aggregates of minerals such as Ca-rich plagioclase, olivine, amphibole and clinopyroxene. In some of the samples, such clusters comprise several (1–3) modal percent.

Xenoliths. Both the porphyry flow (Qoaf) and the domes (Qord) contain abundant xenoliths which range in size from about 25 cm to less than one cm. Xenolith compositions range from 49.8 to 57.6 wt % SiO_2 with no systematic relationship apparent between the compositions of the xenoliths and the host lavas. The andesite porphyry flow and the domes contain similar, and in some cases identical, xenoliths. Xenolith 72201D, which was found in the northern dome, is chemically and texturally the same as 73103C which was found in the porphyry flow (Table 1 and Fig. 8).

The xenoliths are generally alkali rich with the most mafic samples classifiable as hawaiites (49–51 wt % SiO_2) (Fig. 6). A large proportion of them are strictly mugearites and a few are benmoreites. However, all are silica-saturated, hypersthene-normative with the exception of 72201A, which contains minor normative nepheline, and an amphibole cumulate (72201C) entrained in the O'Leary rhyolite dome.

With the exception of the amphibole cumulate, the xenoliths are rounded, fine grained and dominated by intergrown acicular amphibole and plagioclase laths with varying amounts of orthopyroxene, clinopyroxene, titaniferous magnetite and ilmenite, with scattered aggregates of olivine, clinopyroxene and Ca-rich plagioclase. In some samples, interstitial glass is present. Similar observations were made by Moore et al. (1974). Several xenoliths (73103C and 72201D) have quenched (finer grained) rinds where they contact the host lava (Fig. 8). The amphibole cumulate (72201C) contains large oikocrystic amphiboles enclosing euhedral olivine, clinopyroxene, plagioclase and Fe–Ti oxides. The compositions of the phases in the xenoliths (particularly amphibole and pyroxene) are not constant between xenoliths and do not generally match the compositions of the phenocrysts or the disequilibrium textured xenocrysts in the host lavas (Tables 4, 5).

Disequilibrium features are also present in some xenoliths, such as quartz xenocrysts with glass and pyroxene reaction rims, sieve-textured feldspars, and reversely zoned pyroxene and feldspar. For example, 72201D has clinopyroxene with 100 Mg/[Mg + Ca + Fe^{2+}] = 46 at the core to 49 at the rim as well as plagioclase with An_{54} in the core, An_{61} midway, and An_{50} at the rim (Tables 3 and 4, Figs 3 and 4).

The xenoliths, again with the exception of 72201C, are interpreted to be quenched magmas rather than cumulates. Their textures are consistent with moderately rapid cooling to produce the acicular, fine grained fabric together with glass in a few samples. However, glass (sometimes devitrified) could also be indicative of partial melting upon entrainment in the host magma if the xenoliths were completely crystalline at the time of entrainment.

Feldspar xenocrysts. The O'Leary eruptive units and their xenoliths contain abundant sieve-textured, partially melted feldspar xenocrysts that appear to be in disequilibrium with the host rock. There are two types of corroded feldspars with compositions that fall outside the range defined by the euhedral, uncorroded feldspar phenocrysts and the matrix feldspars. Firstly, there are oligoclase feldspars with corroded sieve-textured rims containing (intact) core compositions of An_{12-15} (Figs. 3 and 8e, Table 3). Secondly, andesine feldspars occur with corroded or sieve-textured cores that are in the ranges of An_{30-45} or An_{59-61}. Intact and more albitic rims (An_{19}) typically mantle these cores (Table 3, Figs. 3 and 8f). Analyses of the sieve-textured rim of the oligoclase crystals indicate glass-dominated compositions, i.e., microprobe totals (obtained

Table 3. Representative feldspar analyses

Sample	72902-xenolith				72201D-xenolith				
	Sieve-cored	Matrix	Subhedral core	rim	Sieve-rimmed	Sieve-cored	Matrix	Subhedral core	mid-way
Na_2O	6.81	7.07	5.32	7.24	8.90	4.36	6.61	5.09	4.26
CaO	7.56	7.12	10.47	5.94	2.72	12.44	7.74	10.94	12.36
K_2O	0.40	0.68	0.25	0.62	1.15	0.18	0.51	0.22	0.16
Al_2O_3	26.16	25.13	27.71	24.51	22.34	29.94	25.91	28.78	30.11
Fe_2O_3	0.10	0.32	0.49	0.29	0.07	0.51	0.71	0.47	0.51
SiO_2	58.21	58.96	54.05	60.78	65.69	52.18	58.56	53.93	51.79
Total	99.24	99.28	98.29	99.38	100.87	99.61	100.04	99.43	99.19
An	37	34	51	30	14	61	38	54	61
Ab	61	62	47	66	80	38	59	45	38

Sample	72905-Qord							80305-Qoaf	
	Sieve-cored core	rim	Subhedral	Euhedral core	mid-way	rim	K-spar	Sieve-rimmed	Sieve-cored
Na_2O	7.24	8.45	8.93	8.75	8.23	8.63	3.55	8.15	6.79
CaO	6.65	3.87	2.99	3.11	4.64	3.46	0.11	4.95	7.55
K_2O	0.58	1.18	1.29	1.18	0.84	1.28	11.67	0.88	0.76
Al_2O_3	25.28	22.64	21.87	22.05	23.12	22.21	18.89	23.82	26.14
Fe_2O_3	0.23	0.14	0.14	0.13	0.12	0.06	0.15	0.07	0.24
SiO_2	59.55	62.98	64.63	64.93	61.41	63.38	64.50	61.58	58.43
Total	99.53	99.26	99.85	100.15	98.36	99.02	98.85	99.45	99.91
An	33	19	14	15	23	17	Or_{68}	24	36
Ab	64	74	78	78	73	76	32	71	60

Sample	72802-Qor	Granulite-xenoliths			72206A-Qmac				80304-Qmr
	Euhedral	Subhedral	Subhedral	Subhedral	Euhedral	Sieve-rimmed	Sieve-cored	Matrix	Sieve-rimmed
Na_2O	6.97	4.34	5.56	6.81	3.33	7.90	4.48	4.37	7.18
CaO	7.76	12.32	8.66	6.38	13.90	4.06	11.98	12.29	6.18
K_2O	0.37	0.13	1.37	1.52	0.17	1.94	0.25	0.23	1.09
Al_2O_3	26.24	30.31	26.93	24.59	30.91	22.56	29.25	29.47	24.60
Fe_2O_3	0.30	0.13	0.27	0.44	0.55	0.21	0.50	0.63	0.28
SiO_2	57.74	52.52	57.15	60.25	50.10	62.54	52.30	52.02	60.71
Total	99.38	99.75	99.94	99.99	98.96	99.31	98.76	99.00	100.04
An	37	61	43	31	69	20	59	60	30
Ab	61	39	49	60	30	69	40	39	63

with standards appropriate for feldspar analyses) are low (96–97%) and silica contents are unusually high for feldspar (74 wt %). Several of the rhyolites and dacites (Qord, Qoaf, Qod) contain rapakivi feldspars which have been described by Bladh (1980) and consist of an alkali-feldspar core ($Or_{60}Ab_{33}$–$Or_{65}Ab_{34}$) surrounded by a glassy zone and an outer mantle of plagioclase feldspar (An_{14-15}) (Fig. 3).

Andesite pyroclastic deposit (Qoap). The andesite pyroclastic deposit, which occurs on the flanks of the northern dome, ranges from 56.5 to 58.6 wt % SiO_2 and can be classified as a benmoreite. The deposit is composed of crudely bedded red scoria with abundant xenolithic fragments of the rhyolite dome and the porphyry flow. Samples contain scattered phenocrysts of plagioclase, amphibole and clinopyroxene as well as quartz xenocrysts with pyroxene reaction rims in a glassy red-brown groundmass.

Other O'Leary units. The other O'Leary units, which overlie the Qord and Qoaf flows, contain between 66.4 and 71.6 wt % SiO_2 and are trachytes, alkali rhyolites, and rhyolites. The Deadman Mesa flow (Qor) contains plagioclase and hypersthene microphenocrysts scattered in a microcrystalline to cryptocrystalline orthopyroxene + feldspar + Fe − Ti oxide groundmass. There are rare corroded clinopyroxene and reversely zoned orthopyroxene. The rhyodacite obsidian flow (Qoo) contains small phenocrysts of plagioclase and fayalitic olivine in a groundmass of quartz, fayalitic olivine, minor altered amphibole, apatite and zircon. The dacite flow (Qod) contains reversely zoned orthopyroxene, clinopyroxene,

72201D-xenolith	72201A-xenolith			72201F-xenolith					
rim	Euhedral	Matrix core	rim	Sieve-rimmed	Euhedral core	mid-way	rim	Matrix	Matrix
5.51	4.45	4.54	6.63	9.07	6.48	5.98	6.55	6.27	5.56
10.12	11.95	11.50	7.63	2.85	8.48	9.29	7.97	8.41	10.26
0.28	0.23	0.23	0.62	0.99	0.41	0.37	0.45	0.38	0.32
27.63	29.64	29.28	26.13	22.24	26.71	27.62	26.17	26.96	28.27
0.65	0.56	0.43	0.35	0.12	0.41	0.41	0.51	0.47	0.54
55.34	51.69	52.11	56.95	65.61	57.03	56.05	57.74	57.37	54.76
99.53	98.52	98.09	98.31	100.88	99.52	99.72	99.39	99.86	99.71
50	59	58	37	14	41	45	39	42	50
49	40	40	59	80	57	53	58	56	49

80305-Qoaf			73106-Qoaf				72802-Qor		
Sieve-cored	Euhedral core	rim	Rapakivi core	rim	Sieve-rimmed	Subhedral	Sieve-cored	Sieve-cored	Matrix
6.31	5.21	6.14	3.78	9.07	8.49	6.42	6.52	5.92	7.03
8.73	10.84	9.03	0.17	3.14	4.30	8.47	7.01	9.27	7.20
0.62	0.26	0.45	11.05	1.16	0.90	0.41	0.51	0.33	0.59
26.75	28.38	27.19	18.89	22.31	23.18	26.58	25.62	27.22	25.67
0.34	0.49	0.45	0.11	0.07	0.07	0.31	0.36	0.29	0.66
57.01	54.07	56.76	65.12	64.27	62.97	57.51	58.73	55.81	58.22
99.76	99.25	100.02	99.12	100.02	99.91	99.70	98.75	98.84	99.37
42	53	44	Or_{65}	15	21	41	36	46	35
54	46	54	34	78	74	57	61	53	62

80304-Qmr		80303-Qmr			80401-Qma					
Sieve-rimmed	Matrix	Sieve-rimmed	Matrix	Matrix	Sieve-rimmed	Sieve rimmed	Subhedral core	mid-way	rim	Matrix
7.86	4.54	7.79	5.23	4.26	7.07	7.26	6.51	7.07	6.55	4.44
3.93	12.08	3.81	10.73	12.22	6.68	22.97	8.06	7.13	7.97	11.91
1.48	0.28	1.53	0.34	0.28	1.01	2.00	0.62	0.71	0.62	0.37
22.84	29.67	23.03	28.37	29.28	25.08	22.97	26.34	25.81	26.42	28.88
0.17	0.60	0.21	0.60	0.82	0.24	0.20	0.29	0.22	0.31	0.88
64.38	52.12	64.35	54.65	51.99	59.98	63.54	58.76	59.19	58.08	52.89
100.66	99.29	100.72	99.92	98.85	100.06	100.14	100.58	100.13	99.95	99.37
20	59	19	52	60	32	21	39	34	39	58
72	40	71	46	38	62	67	57	62	58	39

plagioclase and rapakivi K-feldspar. The Robinson Crater dome (Qorr) consists of obsidian and cryptocrystalline to microcrystalline rhyolite with scattered phenocrysts of plagioclase, biotite, and fayalitic olivine.

Strawberry Crater

A wide spectrum of lava compositions has been erupted at Strawberry Crater ranging from 49 to 64 wt % SiO_2. The Strawberry Crater units cross the IUGS alkaline-subalkaline divisor (Fig. 6). The more mafic samples are basalts and basaltic andesites and the more silicic samples are mugearites and benmoreites. All samples are hypersthene-normative.

The basalts contain scattered olivine phenocrysts and microphenocrysts in a microcrystalline groundmass of plagioclase + clinopyroxene + Fe − Ti oxides ± olivine. The andesites and dacites contain orthopyroxene + clinopyroxene + plagioclase phenocrysts and relatively abundant sieve-textured (both sieve-cored and sieve-rimmed) plagioclase xenocrysts in a microcrystalline groundmass of plagioclase + orthopyroxene + Fe − Ti oxides.

Disequilibrium relationships exist between feldspars and pyroxenes in the Strawberry Crater units (Figs. 3 and 4). Some of the Strawberry Crater andesites contain clinopyroxenes with very high Mg content that may be relict from a more primitive basaltic magma. Many phenocrysts in Strawberry Crater samples are characterized by reverse zoning patterns (Table 4, Fig. 4). Sample 80303 (dacite) has orthopyroxene with Mg No. = 57 in the core and 83 in the rim. 72206A (andesite) contains corroded orthopyroxene

Table 4. Representative pyroxene analyses

Sample	72902-Xenolith							72201F-Xenolith		
	Cpx Jacket on qtz	Cpx Jacket on qtz	Opx Jacket on qtz	Opx Jacket on qtz	Opx Matrix	Cpx Matrix	Opx Matrix	Cpx Subhedral	Opx Rounded	Opx Rounded
SiO_2	50.37	50.93	50.96	50.17	51.06	49.81	49.86	48.50	49.66	49.69
TiO_2	0.12	0.17	0.23	0.16	0.20	0.28	0.25	0.99	0.29	0.22
Al_2O_3	0.20	0.30	0.67	0.27	1.18	0.56	0.48	4.85	2.61	1.85
Cr_2O_3	0.00	0.00	0.00	0.00	0.00	0.02	0.00	0.00	0.00	0.13
Fe_2O_3	3.61	3.47	2.68	1.87	1.99	2.06	1.55	5.54	2.93	3.04
FeO	18.98	13.50	23.85	27.94	24.83	22.14	28.79	7.25	24.58	26.68
MnO	1.11	0.67	1.05	1.26	1.00	1.07	1.33	0.27	0.71	0.80
MgO	12.56	12.15	19.22	14.95	19.00	12.78	14.35	13.61	18.42	17.26
CaO	13.30	18.61	1.55	3.38	1.30	10.39	3.33	18.50	1.23	1.14
Na_2O	0.22	0.32	0.05	0.06	0.04	0.16	0.05	0.73	0.05	0.05
Total	100.47	100.12	100.26	100.06	100.60	99.27	99.99	100.24	100.48	100.86
$Mg/Mg+Fe^{2+}$	0.55	0.62	0.59	0.49	0.58	0.52	0.48	0.77	0.58	0.54
$Mg/Mg+Ca+Fe^{2+}$	0.39	0.37	0.57	0.46	0.57	0.39	0.44	0.44	0.56	0.53

Sample	80305-Qoaf	72802-Qor					73001-Qod			
	Opx Reaction rim on olivine	Opx Euhedral core	rim	Opx Matrix	Cpx Corroded	Opx Euhedral	Opx Euhedral core	mid-way	rim	Cpx Subhedra
SiO_2	52.48	50.41	50.78	50.57	51.45	50.49	49.59	49.20	51.41	51.19
TiO_2	0.27	0.13	0.21	0.23	0.18	0.16	0.18	0.09	0.24	0.13
Al_2O_3	1.05	0.89	1.49	1.21	0.62	1.27	0.96	0.62	1.11	0.29
Cr_2O_3	0.03	0.01	0.00	0.02	0.02	0.00	0.00	0.00	0.02	0.02
Fe_2O_3	0.57	1.75	2.52	3.18	4.42	3.49	2.83	2.11	2.58	3.99
FeO	23.27	29.02	23.10	22.35	6.79	22.29	30.26	32.36	23.60	15.74
MnO	0.89	1.53	1.04	1.18	0.69	1.01	1.50	1.81	1.23	1.11
MgO	20.92	15.93	19.69	19.46	15.34	19.97	14.74	13.14	19.44	13.57
CaO	1.40	1.34	1.38	1.99	19.82	1.26	1.20	1.18	1.84	14.92
Na_2O	–	0.02	0.03	0.03	0.32	0.05	0.05	0.04	0.03	0.28
Total	100.88	101.03	100.24	100.22	99.65	99.99	101.31	100.55	101.50	101.24
$Mg/Mg+Fe^{2+}$	0.62	0.50	0.61	0.61	0.80	0.62	0.47	0.42	0.60	0.61
$Mg/Mg+Ca+Fe^{2+}$	0.60	0.48	0.59	0.59	0.46	0.60	0.46	0.41	0.58	0.41

Fe^{2+}/Fe^{3+} calculated from charge balance, based on normalization to 6 cations

with Mg No. = 41 in the core and 78 in the rim. All of the Strawberry Crater samples studied contain sieve-rimmed oligoclase (An_{19-20} and An_{30}) and some andesites contain sieve-cored (An_{59}) xenocrysts. These feldspar xenocrysts are comparable to those present in the O'Leary units (Table 3, Fig. 3).

Vent basalts

The numerous basaltic vents in the region (Fig. 5) have produced lavas with compositions that overlap the most primitive lavas erupted at Strawberry Crater (Table 1). Silica contents of the vent basalts range from 47.1–49.9 wt % SiO_2 and MgO content ranges from 6.7–13.0 wt %. Based on the IUGS alkali content classification, the lavas are generally subalkaline (Fig. 6). Most are olivine basalts with normative olivine and hypersthene, but one sample (73105A) contains a small amount of normative nepheline (Table 2).

Geothermometry

Four xenoliths and one Strawberry Crater sample contain coexisting magnetite and ilmenite phenocrysts and microphenocrysts in the matrix. Temperature estimates were calculated using the Spencer and Lindsley (1981) geothermometer. The temperatures calculated for the xenoliths are 720–800° C for 72201A, 890–930° C for 72201F, 890–1020° C for 72201D, and 1020–1110° C for 72902 (see Table 6 for representative analyses and calculated temperatures). Although there is a fairly large spread within each sample, the temperature ranges for different xenoliths do not overlap much. Surprisingly, the xenoliths that record the highest temperatures are those with the highest silica content and conversely, those with the lowest temperatures are those with the lowest silica content (Tables 1 and 6). This is contrary to what one might expect. However, the magnetite analyses for 72902 are poor (microprobe totals <97%) so the temperatures calculated for 72902 may be erroneous.

72201F-Xenolith	72201D-Xenolith			73106-Qoaf					80305-Qoaf		
Opx Subhedral	Cpx Subhedral core	mid-way	rim	Opx Matrix	Opx Euhedral	Opx Subhedral core	rim	Cpx Corroded	Cpx Subhedral core	rim	Cpx Matrix
47.54	49.26	47.57	49.78	50.12	50.79	49.28	51.62	48.48	51.07	51.08	51.27
0.19	1.05	1.39	0.70	0.18	0.21	0.09	0.19	1.49	0.26	0.32	0.26
2.77	4.16	5.04	3.12	0.60	0.97	0.62	0.46	4.93	0.42	0.96	0.71
0.00	0.00	0.03	0.00	0.04	0.04	0.00	0.00	0.01	0.01	0.00	0.00
2.56	5.19	6.80	5.27	2.92	2.05	1.64	2.71	5.67	3.48	4.01	2.97
35.16	4.81	2.94	4.59	28.99	26.49	34.15	24.77	3.84	12.21	9.49	11.59
1.01	0.28	0.25	0.25	1.47	1.24	1.38	1.09	0.25	0.60	0.45	0.47
10.95	14.79	14.66	15.92	15.73	17.63	12.40	19.26	14.56	13.11	13.80	13.06
0.96	20.23	20.40	19.26	1.29	1.46	1.28	1.48	20.73	18.35	19.39	19.07
0.12	0.53	0.56	0.48	0.06	0.04	0.04	0.02	0.57	0.36	0.44	0.40
101.26	100.30	99.64	99.37	101.40	100.92	100.88	101.60	100.53	99.87	99.94	99.80
0.36	0.85	0.90	0.86	0.50	0.55	0.40	0.59	0.87	0.66	0.73	0.67
0.35	0.46	0.47	0.49	0.48	0.53	0.37	0.57	0.46	0.40	0.42	0.39

73001-Qod		80303-Qmr					80401-Qma	72206A-Qmac				
Cpx Suhedral	Opx Euhedral	Opx Euhedral	Cpx Subhedral	Cpx Elongate	Opx Subhedral core	rim	Cpx Subhedral	Cpx Subhedral core	rim	Cpx Matrix	Cpx Euhedral	Opx Reaction rim on olivine
51.39	50.05	50.34	50.43	50.39	51.00	53.91	51.47	49.64	53.55	51.49	48.74	52.34
0.14	0.27	0.18	0.56	0.60	0.12	0.28	0.62	0.11	0.14	0.39	0.64	0.17
0.28	2.33	0.62	4.77	4.50	0.52	1.52	3.66	0.46	0.86	3.19	5.87	0.30
0.02	0.00	0.00	0.20	0.14	0.00	0.06	0.14	0.00	0.02	0.18	0.31	0.00
4.51	4.31	1.85	4.69	5.42	3.25	4.21	0.12	2.51	4.71	4.05	6.10	0.01
13.82	22.29	30.42	0.76	0.36	25.29	10.94	5.12	34.10	13.83	1.87	0.23	25.44
1.02	1.08	1.30	0.14	0.10	1.10	0.39	0.14	1.21	0.53	0.11	0.15	0.67
13.38	19.64	15.14	16.63	16.72	18.46	28.46	15.32	12.66	26.84	17.49	16.00	18.35
17.01	1.38	1.36	22.13	22.19	1.45	1.95	21.89	1.21	1.45	21.39	21.77	1.76
0.26	0.04	0.06	0.39	0.43	0.05	0.04	0.30	0.02	0.05	0.27	0.42	0.02
101.83	101.39	101.27	100.70	100.85	101.24	101.76	98.78	101.92	101.98	100.43	100.23	99.06
0.64	0.62	0.47	0.98	0.99	0.57	0.83	0.84	0.41	0.78	0.94	0.99	0.56
0.40	0.60	0.46	0.51	0.51	0.55	0.79	0.45	0.40	0.76	0.52	0.50	0.54

One possible explanation for the observed relationship between calculated temperature and silica content is that the coexisting oxides were not in equilibrium. This would be consistent with the abundant disequilibrium features observed in the samples (e.g., xenocrysts, reverse zoning). Another possibility is that the temperatures are not those of the hybrid melt. Perhaps the calculated temperatures are relict from the basalt in which the oxides may have originally formed. The large ratio of rhyolite to basalt in the mixture may have inhibited reequilibration due to increased viscosity and decreased diffusion rates in the cooler, more silicic hybrids. Conversely, diffusion may have continued to a lower temperature in the more fluid basaltic hybrids. Coexisting Fe–Ti oxides were found only in one Strawberry Crater sample: 80303. The temperature calculated for this sample is 840–890° C which is consistent with the high silica content of the sample (64 wt %). Coexisting orthopyroxene and clinopyroxene phenocrysts are clearly not in equilibrium (Fig. 4) and two-pyroxene thermometry produces meaningless values.

Geochemistry

O'Leary Peak

Harker-type diagrams show that the major and trace element concentrations for a subset of the O'Leary Peak suite covary linearly with SiO_2 and MgO (Fig. 9). This subset includes (in order of decreasing silica) the O'Leary northern dome (Qord), Darton Dome (Qord), the andesite porphyry flow (Qoaf), the andesite pyroclastic deposit (Qoap) and the andesitic and basaltic xenoliths. These linear variations also exist within units that exhibit a range of compositions (eg. Qoaf).

Compositional ranges of some of the units overlap. Darton Dome sample 72909 (Qord) is compositionally identical in both major and trace element abundances (within analytical precision) to Qoaf sample 73107 (Table 1). The most

Table 5. Representative amphibole analyses

Sample	72902-Xenolith			72201A-Xenolith		72201D-Xenolith		
	Subhedral	Euhedral	Matrix	Rounded	Matrix	Core	Rim	Matrix
SiO_2	38.36	37.56	37.90	40.75	39.49	38.62	36.60	37.70
TiO_2	4.75	5.20	3.82	2.53	1.85	4.54	4.86	4.72
Al_2O_3	12.69	13.71	12.90	10.59	11.27	13.33	14.55	13.05
Fe_2O_3	7.44	8.63	10.21	9.74	12.27	10.35	7.40	10.32
FeO	5.70	4.37	7.82	8.09	6.77	7.32	12.92	3.98
MnO	0.17	0.13	0.39	0.48	0.46	0.22	0.30	0.21
MgO	13.26	13.55	10.42	11.63	11.61	10.98	8.21	13.07
CaO	10.98	11.04	10.20	10.65	10.75	10.17	10.90	10.52
Na_2O	2.69	2.81	2.70	2.40	2.35	2.84	2.74	2.76
K_2O	0.60	0.54	0.68	0.98	1.08	0.66	0.69	0.66
F_2	0.34	0.14	0.16	0.22	0.30	0.50	0.14	0.24
Cl_2	0.02	0.01	0.05	0.05	0.02	0.02	0.04	0.00
H_2O	1.85	1.96	1.90	1.89	1.85	1.79	1.91	1.90
Total	98.70	99.58	99.06	99.90	99.93	101.11	101.19	99.01

Sample	72201F-Xenolith		73106-Qoaf		72905-Qord		73001-Qod
	Core	Rim	Matrix	Euhedral	Matrix	Matrix	Euhedral
SiO_2	37.60	38.34	38.78	39.99	41.20	39.58	40.52
TiO_2	4.74	3.79	4.57	1.15	3.67	3.92	2.73
Al_2O_3	13.44	13.25	13.19	9.31	10.83	12.77	11.20
Fe_2O_3	9.83	11.57	9.04	11.05	10.67	8.16	12.87
FeO	6.95	4.90	7.51	17.68	4.52	7.34	5.96
MnO	0.19	0.17	0.19	1.15	0.28	0.30	0.47
MgO	11.12	12.27	11.56	4.87	13.61	11.95	11.40
CaO	10.14	10.35	10.36	9.97	10.21	10.67	9.90
Na_2O	2.85	2.82	2.90	2.09	2.92	2.74	2.59
K_2O	0.72	0.75	0.73	1.09	0.52	0.61	0.55
F_2	0.28	0.09	0.18	0.37	2.46	1.51	0.25
Cl_2	0.02	0.03	0.01	0.17	0.00	0.01	0.03
H_2O	1.87	1.98	1.95	1.70	0.89	1.31	1.90
Total	99.64	100.25	100.87	100.39	100.73	100.22	100.25

Fe^{2+}/Fe^{3+} calculated from charge balance, based on normalization to 22 oxygens
H_2O content calculated assuming $OH^- + F^- + Cl^- = 2.00$

mafic pyroclastic sample, 72203A, is chemically identical within analytical precision to one of the xenoliths found in the Darton Dome (72902) (Table 1). This is significant because as a pyroclastic scoria deposit, 72203A clearly has a magmatic origin and its composition suggests that the xenolith 72902 is a sample of the same magma. This supports the hypothesis that the xenoliths are magmatic inclusions and not cumulates.

Silica variation diagrams show that the xenoliths are relatively rich in TiO_2, Na_2O, and Fe_2O_3 and poor in MgO and CaO compared to the other mafic units in the area (Strawberry Crater basalts and other vent basalts) (Fig. 9). Similarly, the xenoliths have very different trace element concentrations than the Strawberry Crater suite and the other basaltic vents sampled. In general, the xenoliths display an evolved signature with low concentrations (relative to the vents) of Sc (10–17 ppm), V (50–142 ppm) and a striking depletion in Ni (0–5 ppm) and Cr, which is present in concentrations below the detection limits in our routine XRF analysis technique (Table 1). In addition, the xenoliths have higher concentrations of Rb (14–44 ppm) and Zr (249–351 ppm) and lower Ba (587–825) than the vents.

The most silicic unit in the O'Leary suite is Qorr (an alkali rhyolite) with 71.6 wt % SiO_2 and correspondingly high K_2O and Na_2O and low CaO, MgO, total Fe, and TiO_2 concentrations. Samples from Qor, Qod and Qoo also have high silica contents. These four units have trace element abundances that are distinct in comparison with the other O'Leary units of similar major element chemistry. For example, samples from Qorr, Qor, and Qoo all have higher Zr, Ba and MnO contents than Qord or Qoaf samples of equal silica content (Table 1, Fig. 9).

Strawberry Crater

Most of the major and trace element concentrations of the Strawberry Crater suite vary colinearly with SiO_2 and MgO (Fig. 9). Major and trace element concentrations for samples from Strawberry Crater define a distinctly different trend from the O'Leary trend. An AFM diagram for the O'Leary and Strawberry suites shows the non-tholeiitic nature of the two suites (Irvine and Baragar 1971) and the distinct differences between them (Fig. 10).

Table 6. Representative Fe–Ti oxide analyses and geothermometry using Spencer and Lindsley 1981

	72902-Xenolith			
	Mag	Mag	Ilm	Ilm
SiO_2	0.08	0.13	0.04	0.05
TiO_2	18.35	20.04	47.37	46.56
Al_2O_3	1.85	1.75	0.13	0.15
Cr_2O_3	0.4	0.00	0.00	0.00
Fe_2O_3	29.11	25.98	10.17	11.42
FeO	45.40	47.03	38.86	38.65
MnO	0.59	0.59	0.74	0.57
MgO	0.88	0.88	1.69	1.49
CaO	0.03	0.06	0.03	0.04
Total	96.69	96.46	99.01	98.91
X_{usp}	0.57	0.62	–	–
X_{hem}	–	–	0.10	0.11

Calc. Temp.: 1020–1110 C
Log fO_2 = −9.5 to −10.4
Delta FMQ = −0.1 to 0.3

	72201A-Xenolith			
	Mag	Mag	Ilm	Ilm
SiO_2	0.10	0.15	0.05	0.05
TiO_2	18.24	13.83	50.81	51.92
Al_2O_3	2.61	2.48	0.06	0.10
Cr_2O_3	0.01	0.00	0.00	0.00
Fe_2O_3	29.63	38.47	5.56	3.59
FeO	45.63	42.63	40.34	38.84
MnO	0.66	0.44	0.91	1.08
MgO	1.07	0.64	2.50	3.78
CaO	0.02	0.05	0.02	0.04
Total	97.97	98.68	100.26	99.40
X_{usp}	0.57	0.43	–	–
X_{hem}	–	–	0.06	0.04

Calc. Temp.: 720–800 C
Log fO_2 = −16.8 to −16.5
Delta FMQ = −0.7 to −0.4

	80303-Qmr Strawberry Crater			
	Mag	Mag	Ilm	Ilm
SiO_2	0.12	0.25	0.02	0.01
TiO_2	14.30	16.34	47.93	49.08
Al_2O_3	2.42	1.42	0.23	0.16
Cr_2O_3	0.02	0.04	0.02	0.05
Fe_2O_3	39.91	34.24	11.13	8.00
FeO	41.38	43.38	36.58	38.99
MnO	0.42	0.43	0.51	0.51
MgO	2.16	1.37	3.36	2.58
CaO	0.01	0.11	0.02	0.03
Total	100.73	97.56	99.80	99.41
X_{usp}	0.42	0.49	–	–
X_{hem}	–	–	0.11	0.08

Calc. Temp.: 840–890 C
Log fO_2 = −12.0 to −13.6
Delta FMQ = 0.1 to 0.9

Fe^{2+}/Fe^{3+} calculated assuming 3 cations and 4 oxygens for magnetite, and 2 cations and 3 oxygens for ilmenite. Activities and X_{usp} and X_{hem} were calculated using the mixing model for Stormer (1983). $X_{usp} + X_{mt} = 1$; $X_{hem} + X_{ilm} = 1$

Table 6 (continued)

	72201F-Xenolith			
	Mag	Mag	Ilm	Ilm
SiO_2	0.08	0.11	0.04	0.05
TiO_2	19.28	19.01	49.45	49.17
Al_2O_3	3.48	3.41	0.06	0.07
Cr_2O_3	0.00	0.00	0.00	0.00
Fe_2O_3	26.88	27.70	6.46	6.93
FeO	46.60	46.30	40.30	39.99
MnO	0.55	0.56	0.63	0.64
MgO	1.26	1.28	2.00	2.02
CaO	0.00	0.13	0.01	0.03
Total	98.13	98.50	98.95	98.90
X_{usp}	0.62	0.61	–	–
X_{hem}	–	–	0.07	0.07

Calc. Temp.: 890–930 C
Log fO_2 = −12.5 to −13.3
Delta FMQ = −0.5 to −0.6

	72201D-Xenolith			
	Mag	Mag	Ilm	Ilm
SiO_2	0.08	0.11	0.00	0.05
TiO_2	16.91	16.39	47.67	49.14
Al_2O_3	5.66	5.31	0.18	0.13
Cr_2O_3	0.00	0.01	0.05	0.01
Fe_2O_3	30.27	30.89	9.97	7.12
FeO	42.58	41.90	36.22	37.14
MnO	0.51	0.54	0.56	0.51
MgO	2.82	2.75	3.38	3.6
CaO	0.06	0.01	0.04	0.10
Total	98.89	97.90	98.06	97.82
X_{usp}	0.56	0.54	–	–
X_{hem}	–	–	0.10	0.07

Calc. Temp.: 890–1020 C
Log fO_2 = −10.4–13.3
Delta FMQ = −0.2 to 0.3

The Strawberry Crater basalts appear to have more primitive major and ferromagnesian compatible trace element signatures than the O'Leary basaltic xenoliths. The Strawberry basalts have 8.1–7.6 wt % MgO, compared to 4.6–3.4% in the basaltic xenoliths. Similarly, Strawberry basalts contain 215–286 ppm V, 29–30 ppm Sc, 155–241 ppm Cr, and 69–83 ppm Ni, all considerably higher than the O'Leary basaltic xenoliths. However, some of these elements are present in lower abundances in Strawberry Crater basalts than in the nearby basaltic vents, which contain up to 13 wt % MgO, 265 ppm Ni and 995 ppm Cr. The Strawberry basalts also have distinctly higher Ce/Y (6.2–6.8) than the O'Leary basaltic xenoliths (2.4–2.9), and no simple fractional crystallization relationship exists between these two groups.

Least-squares mixing models

Major and trace element trends can be used to evaluate the possible roles of assimilation, fractional crystallization, and magma mixing in the genesis of the O'Leary and Strawberry Crater volcanics (Allegre and Minster 1978; DePaolo

Table 7. Representative olivine analyses

Sample	72201D Xenolith Subhedral	72201F Xenolith Matrix	73106 Qoaf with pyx rim	73007 Qoo Euhedral fayalite	80401 Qma Euhedral	72206A Qmac Euhedral
SiO_2	38.06	35.08	37.59	30.94	40.73	39.34
TiO_2	0.04	0.07	0.01	0.00	0.03	0.33
Al_2O_3	0.04	0.03	0.02	0.00	0.03	0.04
Cr_2O_3	0.00	0.02	0.03	0.00	0.02	0.03
FeO	24.57	40.79	26.67	62.47	14.71	16.66
MnO	0.39	0.83	0.47	2.57	0.21	0.21
MgO	36.76	23.16	35.59	3.83	44.21	42.57
CaO	0.16	0.17	0.18	0.12	0.23	0.20
Total	100.02	100.15	100.56	99.93	100.17	99.38
$Mg/Mg+Fe^{2+}$	0.73	0.50	0.70	0.10	0.84	0.82

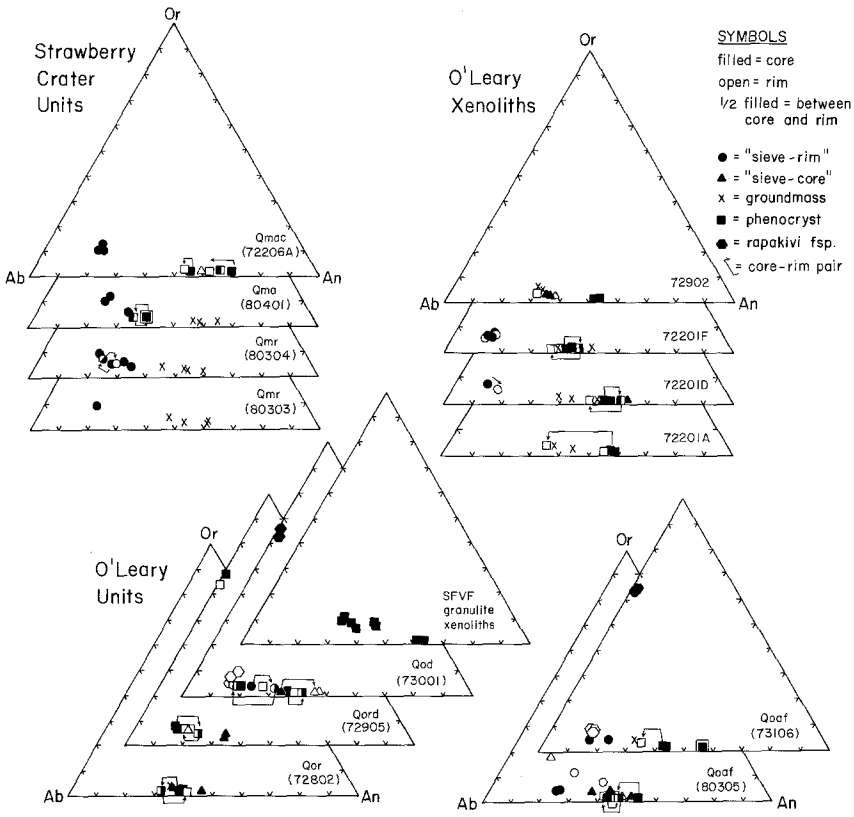

Fig. 3. Representative plagioclase compositions for samples from O'Leary Peak, Strawberry Crater and granulite xenoliths from the SFVF. Feldspar types (sieve-cored, sieve-rimmed, euhedral or subhedral phenocryst, rapakivi or groundmass) are indicated by symbol shape. The location of the analysis relative to the grain boundary (core, rim, or mid-way) is indicated by *solid* and *open symbols*. *Arrows* link analyses from the same grains and show direction of zoning from core to rim

1981; Langmuir et al. 1978; Grove et al. 1982). The most striking aspect of the geochemical trends is that the major and trace element concentrations show a distinct linear variation with SiO_2 and MgO content for Strawberry Crater and for a subset of the O'Leary suite (Fig. 9). Furthermore, the O'Leary suite and the Strawberry Crater suite define two distinctly different geochemical trends (Figs. 9 and 10).

O'Leary Peak

Close examination shows that the major element data for the mafic xenoliths (72201A or 72201B) and the northern dome rhyolite (72204) define a line in composition space which contains many of the other O'Leary units: the Darton Dome (Qord), the andesite porphyry flow (Qoaf), the andesite pyroclastic deposit (Qoap), and the more silicic xenoliths (although there is considerable scatter within the xenolith population for some elements) (Fig. 9). Further examination shows that trace element variations are also linear for these units, as is evident in plots of Rb, Sc, V, and Ba vs SiO_2 or MgO (Fig. 9).

The possibility that binary mixing has resulted in the chemical spectrum is suggested by the linearity of the major element variations. However, major element geochemical variations are not necessarily very sensitive to fractionation versus mixing processes, whereas trace element abundance variations can be used to more clearly determine the contributing effects of fractional crystallization, mixing, or assimilation in the geochemical evolution of a suite of volcanics (Langmuir et al. 1977; DePaolo 1981; Allegre and

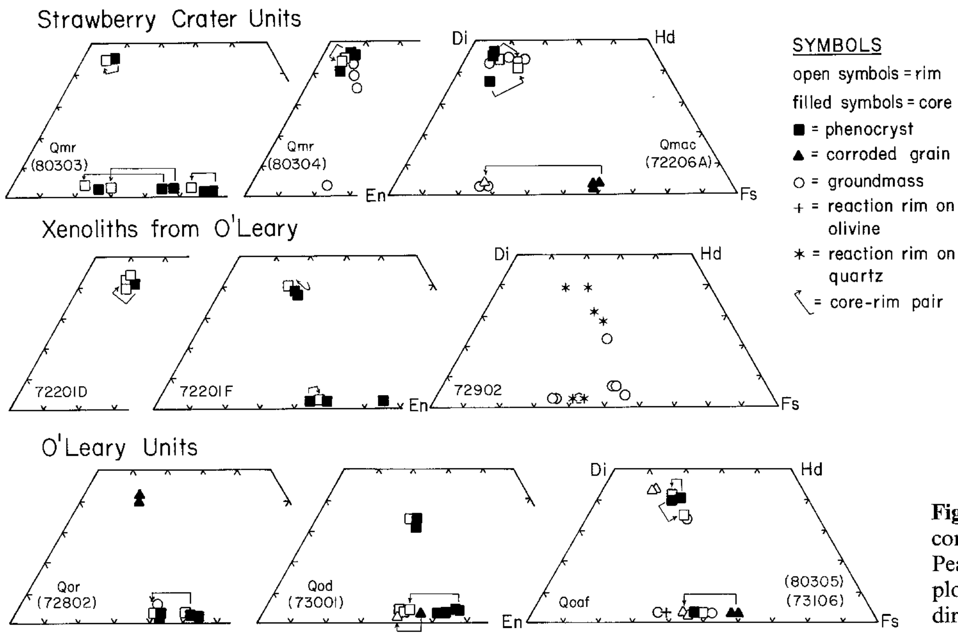

Fig. 4. Representative pyroxene compositions for samples from O'Leary Peak and Strawberry Crater. All Fe is plottted as Fe^{2+}. Arrows indicate direction of zoning from core to rim

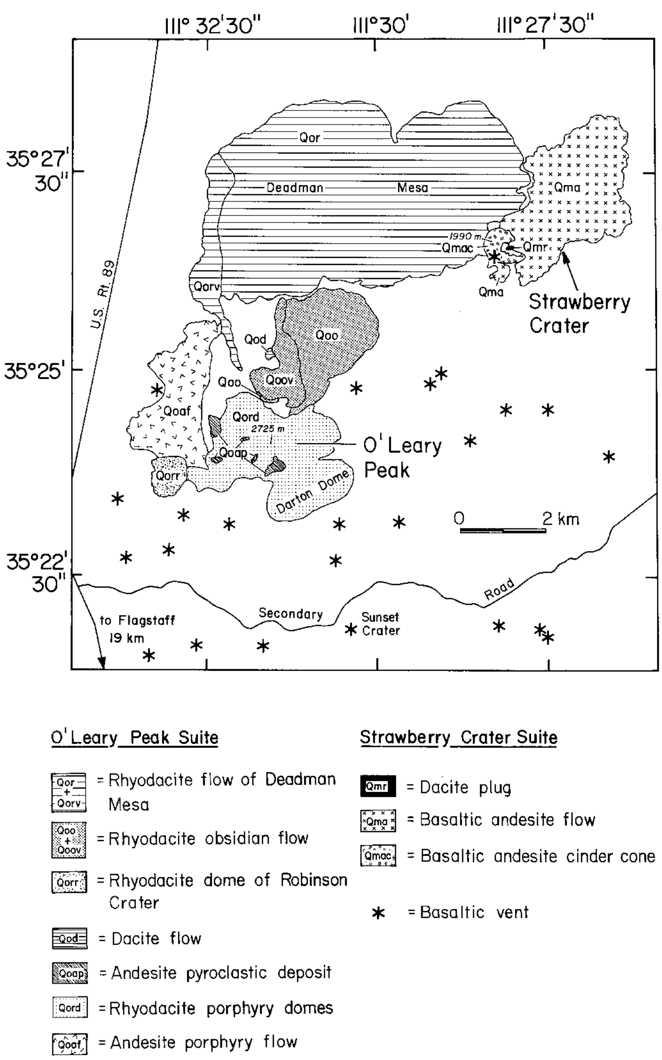

Fig. 5. Geologic map of O'Leary Peak and Strawberry Crater (after Moore and Wolfe 1976)

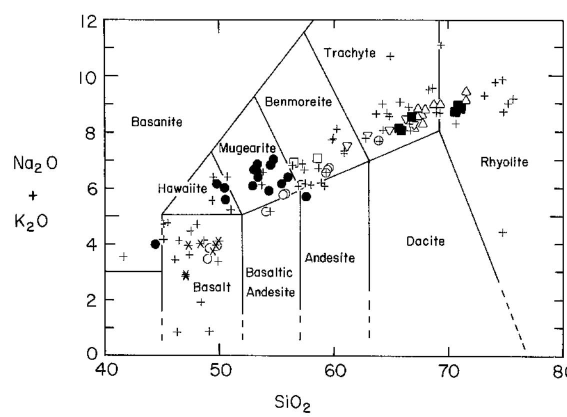

Fig. 6. Total alkali wt % vs silica wt % for samples from O'Leary Peak, Strawberry Crater, and nearby vents shown with data from the USGS (Moore and Wolfe [1987], Newhall et al. [1987], Ulrich and Bailey [1987], Wolfe et al. [1987a], Wolfe et al. [1987b]). *Solid circles* are xenoliths from O'Leary Peak (this study), + = USGS data, and the other symbols are the same as in Fig. 9

Minster 1978; Grove et al. 1982). The observed trace element variations are suggestive of binary mixing and suggest that the northern dome and the mafic xenoliths are possible end-members.

A least-squares mass balance mixing model for major element abundances (Le Maitre 1981) has been used to determine if bimodal mixing could account for the major element compositions of the more silicic xenoliths and the andesitic and dacitic O'Leary lavas and if so, to determine the probable end-member compositions and the relative proportions necessary to produce the various intermediate lavas. This approach was also used to evaluate the alternative possibility that fractionation of the phenocryst phase assemblage identified in the mafic xenoliths could generate the compositions of the intermediate lavas, the intermediate xenoliths or the O'Leary dome rhyolite.

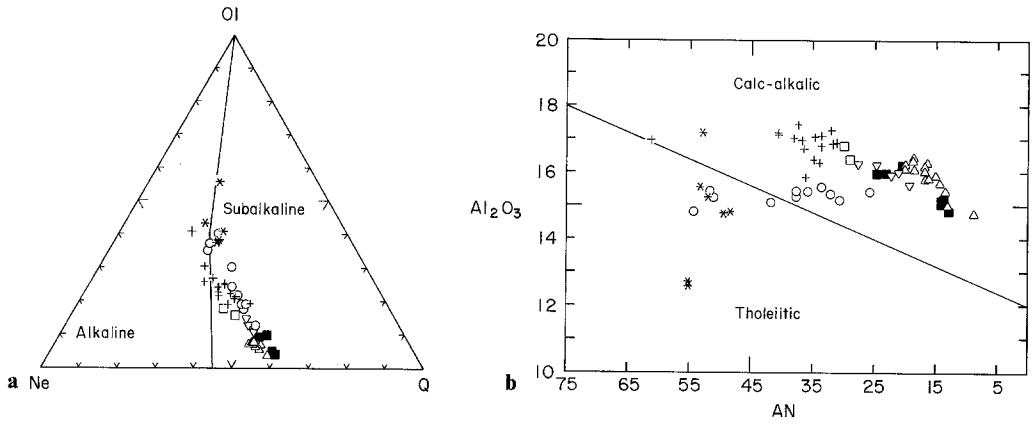

Fig. 7. **a** Normative mineralogy (olivine, nepheline, quartz) of the samples in this study, showing the alkaline-subalkaline fields of Irvine and Baragar (1971). **b** Alumina wt % versus normative An content showing the tholeiitic and calc-alkaline fields of Irvine and Baragar (1971). Symbols are the same as in Fig. 9

Table 8. Least squares modeling calculations

	1	2	3	4	5	6	7	8
Mafic end-member[a]	72201B	72201B	72201B	72201B	72201B	80302G	80302G	80302G
Silicic end-member[a]	Qord[b]	Qord	Qord	Qord	Qord	Qord	Qord	Qord
Hybrid[a]	72902	72203G	80305	Darton[c]	73107	72206C	80403	80303
% Silicic component	29.3	39.9	52.7	77.2	81.0	31.5	47.8	68.7
Residuals[d]								
(wt %)								
SiO_2	0.02	−0.04	0.00	0.06	0.00	0.21	0.18	0.10
TiO_2	0.06	0.03	0.07	0.10	0.05	−0.02	−0.08	−0.02
Al_2O_3	−0.47	−0.21	−0.27	−0.59	−0.58	−0.15	−0.35	−0.27
Fe_2O_3	0.06	−0.01	0.07	0.21	0.08	0.20	0.06	0.22
MnO	−0.01	−0.01	−0.01	0.00	0.00	0.00	0.00	0.01
MgO	0.07	0.10	−0.05	0.02	−0.08	0.27	0.27	−0.05
CaO	0.13	−0.08	0.01	0.00	0.12	−0.02	0.09	−0.01
Na_2O	−0.15	−0.14	0.06	0.13	0.13	−0.18	−0.09	0.00
K_2O	0.16	0.20	−0.01	−0.19	−0.05	−0.21	−0.22	−0.42
P_2O_5	−0.12	−0.12	−0.08	−0.01	−0.04	0.00	−0.02	0.01
Sum r^2	0.32	0.14	0.10	0.46	0.38	0.26	0.30	0.32
Residuals[d] (model concentrations in parentheses)								
(ppm)								
Nb	−3 (34)	−3 (35)	−2 (36)	−2 (37)	0 (38)	6 (41)	6 (40)	12 (40)
Zr	−64 (248)	−71 (247)	−70 (247)	−52 (246)	−44 (246)	−48 (218)	−65 (241)	−94 (232)
Y	−4 (26)	−3 (26)	−2 (25)	−3 (23)	−3 (23)	2 (21)	3 (21)	5 (22)
Sr	−12 (720)	22 (652)	10 (569)	4 (412)	19 (387)	3 (621)	−28 (537)	0 (428)
Th	−2 (4)	1 (6)	0 (7)	−1 (11)	−1 (11)	−3 (12)	1 (13)	−1 (13)
Pb	2 (8)	4 (9)	0 (10)	0 (12)	0 (13)	2 (9)	3 (10)	3 (12)
Zn	−1 (60)	−7 (58)	−3 (54)	−4 (48)	−6 (47)	6 (65)	3 (60)	8 (53)
Cu	0 (0)	0 (0)	0 (0)	0 (0)	0 (0)	−36 (11)	−20 (8)	−4 (5)
Ni	2 (2)	2 (2)	0 (1)	0 (1)	0 (1)	7 (57)	3 (43)	4 (26)
Rb	3 (29)	−1 (33)	0 (39)	2 (50)	5 (52)	8 (27)	12 (35)	14 (45)
Cr	0 (0)	0 (0)	0 (0)	0 (0)	0 (0)	50 (165)	0 (126)	9 (75)
Ce	−10 (77)	−9 (78)	−7 (80)	−2 (83)	−5 (84)	1 (125)	2 (116)	−3 (104)
Sc	−1 (13)	0 (11)	−1 (9)	0 (5)	2 (5)	3 (21)	3 (17)	1 (11)
Nd	−18 (20)	−10 (19)	−8 (19)	−5 (18)	−11 (17)	−3 (34)	−5 (30)	1 (24)
Ba	−42 (783)	31 (838)	−18 (906)	−83 (1034)	−95 (1054)	−36 (1064)	−121 (1086)	−127 (1113)
V	27 (80)	19 (69)	20 (55)	11 (28)	5 (24)	−1 (148)	5 (114)	4 (70)
La	−4 (44)	4 (46)	−3 (47)	−7 (51)	1 (51)	0 (75)	−5 (70)	−12 (63)

[a] see Table 1 for sample compositions
[b] *Qord* average of 71902, 72204, 72205A
[c] *Darton* average of 72903, 72904, 72909
[d] *residual* calculated wt % (or ppm) of model − measured wt % (or ppm) of proposed hybrid

A good fit was obtained between the observed intermediate lava compositions (Qoap, Qoaf, Darton Dome) and a binary mixture of the northern dome rhyolite with a basaltic xenolith (72201B). By varying proportions of this mixture, the compositions of samples of Qoap, Qoaf, and Darton Dome were successfully reproduced (Table 8). In general, the modeled oxide concentrations were within analytical precision of measured concentrations for most of the major oxides. However, the calculated values for Al_2O_3 and CaO differ from the measured values by 1%–5% of the measured weight % and Na_2O and K_2O differ by up to 15%. This suggests that the compositions may reflect the presence of excess feldspar from crustal assimilation (by either the mafic or felsic magma) or by feldspar accumulation in the magma chamber. The ubiquitous presence of disequilibrium feldspar xenocrysts appears to be consistent with either processes of assimilation or accumulation. The presence of excess feldspar might be expected to affect the Ba, Rb, and Sr concentrations such that the abundances of these trace elements would be inconsistent with the mixing model.

As an example of the modeling procedure, the composition of the andesite pyroclastic deposit sample 72203G can be duplicated using a mixture of 60.1% 72201B (basalt) with 39.9% northern dome composition (rhyolite) (Table 8, Model 2). Similarly, the most mafic sample of the andesite porphyry flow, 80305 at 61.2% SiO_2, can be modeled with a mix of 47.3% 72201B and 52.7% northern dome (Table 8, Model 3), the Darton Dome composition can be modeled with a mixture of 22.8% 72201B and 77.2% northern dome (Table 8, Model 4) and the most silicic sample from the andesite porphyry flow, 73107, can be duplicated using a mixture of 19.0% 72201B and 81.0% northern dome (Table 8, Model 5).

Intermediate compositions with an apparent binary mixing signature could be an artifact of the analytical procedures if samples from the units that contain abundant xenoliths were analyzed without removal of the xenolithic material. However, it is unlikely that the observed linear trends are due to lax preparation technique because of the large volume of extraneous xenolithic material that would have to have been overlooked during sample preparation. Least squares mixing models using major element chemistry suggest that the chemical differences between Darton Dome and the northern dome could result from the addition of between 21–32 wt % xenolithic material (based on the range of xenolithic compositions found). Similarly, the andesite porphyry flow (Qoaf), would require as much as 47% xenolithic contamination. We maintain that such a substantial volume would *not* have been overlooked and that the xenolithic content was reduced to a minimum during sample hand-picking.

9	10	11	12
80302G	80302G	80302G	80302G
80303	80303	80303	80303
80401	72206C	72206A	80403
33.3	45.9	55.2	69.5
−0.04	0.16	0.23	0.11
−0.01	−0.02	−0.01	−0.07
0.32	−0.02	−0.02	−0.16
0.05	0.09	0.06	−0.10
0.00	0.00	0.00	0.00
−0.30	0.30	0.41	0.31
0.12	−0.01	0.09	0.10
−0.03	−0.18	−0.14	−0.09
−0.02	−0.02	−0.01	0.07
0.02	0.00	0.01	−0.03
0.21	0.16	0.25	0.17
1 (37)	0 (35)	0 (34)	−1 (32)
−4 (245)	−4 (261)	−14 (272)	−17 (289)
1 (19)	0 (19)	1 (19)	0 (18)
25 (666)	3 (621)	−42 (558)	−28 (537)
−2 (12)	8 (13)	0 (13)	1 (13)
3 (8)	1 (8)	1 (8)	1 (8)
4 (65)	2 (61)	4 (58)	−3 (54)
−8 (14)	−35 (13)	−15 (12)	−17 (11)
−16 (63)	3 (53)	−10 (49)	13 (41)
1 (18)	2 (20)	0 (22)	1 (24)
56 (183)	39 (154)	51 (144)	82 (119)
16 (131)	1 (125)	6 (123)	4 (118)
−1 (23)	3 (21)	6 (19)	2 (16)
−2 (35)	−4 (33)	−5 (32)	−6 (29)
2 (1095)	23 (1123)	−38 (1143)	−33 (1174)
6 (165)	−3 (146)	20 (133)	2 (111)
1 (82)	5 (80)	5 (79)	3 (78)

Trace element modeling for O'Leary Peak

A binary mixing model based on major element chemistry may be tested by how well it can account for the observed trace element abundances. Whereas fractional crystallization typically results in non-linear element-element variations for elements with different bulk distribution coefficients, binary mixing should result in linear element-element variations for all elements (Allegre and Minster 1978; Langmuir et al. 1978).

Trace element abundances for the intermediate lavas (Qoaf, Qoap, Darton Dome) were calculated based on the end-member melt proportions of basalt (72201B) and rhyolite dome determined from the major element mixing models (above), and these calculated values are compared to observed trace element abundances in the samples (Table 8). An excellent fit between the modeled values and the measured values was obtained for the elements Sr, Rb, Sc, Th, Ba, Nb, La, Zn, Ce and Y, which is a clear indication that the lavas of the andesite porphyry flow, andesite pyroclastic deposit, the Darton Dome and the more silicic xenoliths are the products of binary mixing between a basalt like 72201B and the northern dome rhyolite. The fit of Ba, Rb, and Sr with the model indicates that either excess feldspar is not a source of the modeling error for Na_2O, K_2O, CaO and Al_2O_3, or the concentrations of these trace elements in the excess feldspar are not large enough to significantly alter the trace element abundances in the resulting hybrid magma.

Other trace elements fit the model within analytical ac-

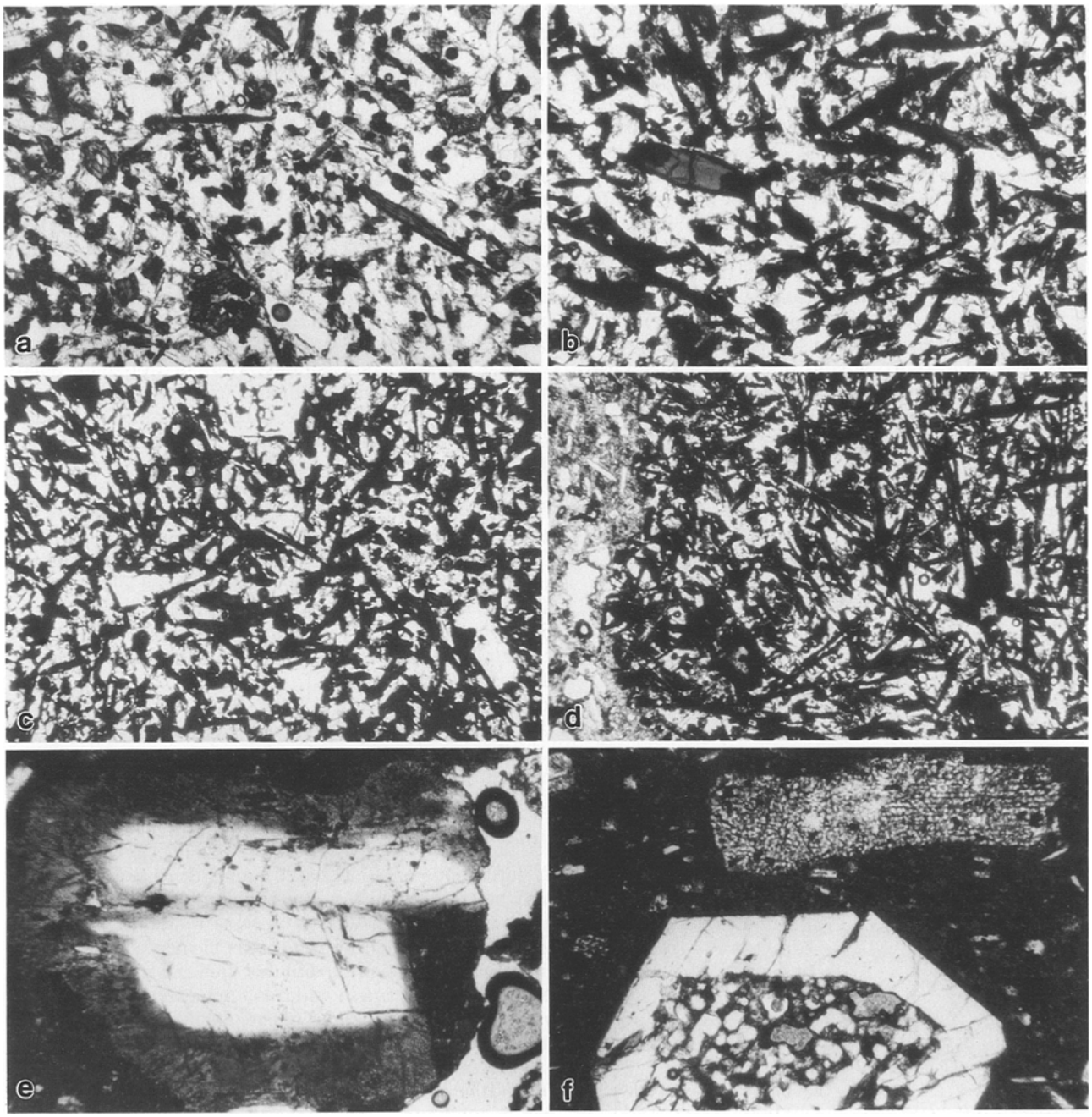

Fig. 8a–f. a–d Photomicrographs of two chemically identical and texturally similar xenoliths, found in different O'Leary units. **a** and **b** are the core and rim respectively of sample 73103C which was entrained in Qoaf. **c** and **d** are the core and rim areas respectively of 72201D which was entrained in Qord. The host is on the left of the contact shown in **d**. The dark acicular crystals are amphibole and the lighter crystals are plagioclase. Note the rim areas (**b, d**) are finer grained and appear to have more acicular (quench-textured) amphiboles than the core areas (**a, c**). The rim area of 73103C is less vesiculated than the core in hand sample. These textures suggest that the xenoliths were magmas that quenched when mixed with the cooler rhyolitic host. The width of the photographs = 2 mm. **e, f** Photomicrographs of the two types of disequilibrium feldspars. **e** Sieve-rimmed feldspar with corroded rim and intact core (An_{12}) (grain is 1 mm long). **f** Two sieve-cored feldspars, both with corroded cores and one with an intact rim overgrowth that is much less calcic (An_{19}) than the core (An_{40}). The width of the photograph = 2 mm

curacy, with the exception of Zr, Nd and V. The modeled Zr content of the mixtures is consistently lower than the actual Zr content of the intermediate rocks, and the Zr content of one or both of the end-members used in the model may be lower than that of the actual end-member(s). The variation of Zr with silica is generally linear (Fig. 9), but 72201B does not appear to be a suitable end-member. Similarly, V content in 72201B is too high to fit the mixing model and Nd content is too low. The general linear variation of these elements with silica supports the mixing model, but the chemistry of the end-member basalt is not exactly represented by xenolith 72201B.

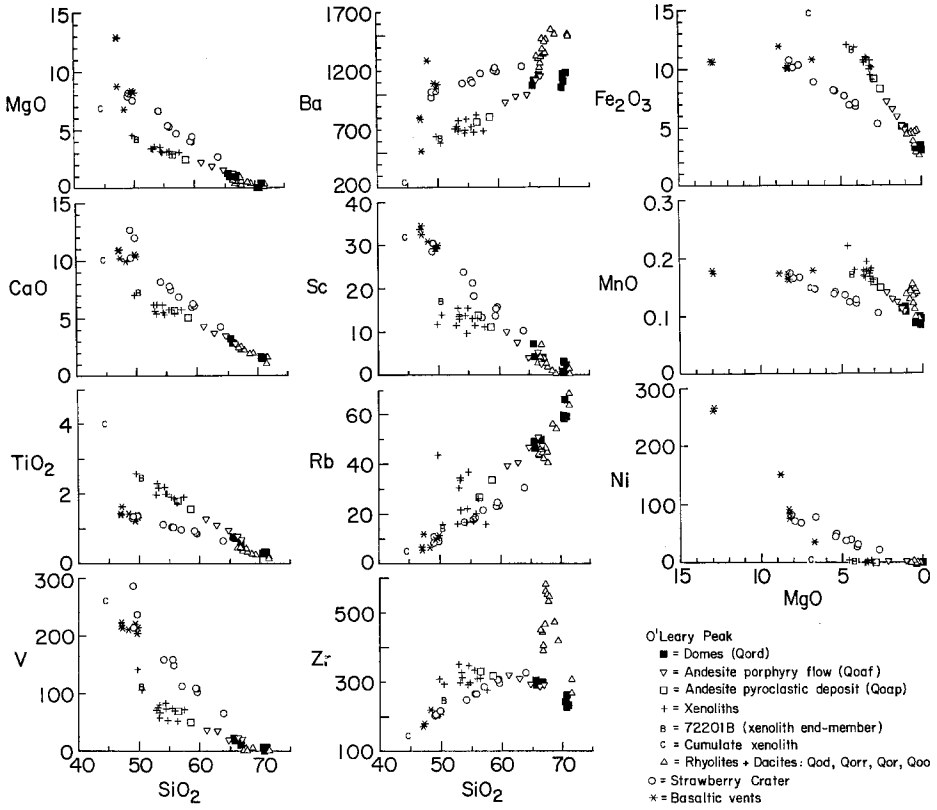

Fig. 9. Selected silica and MgO variation diagrams for samples from O'Leary Peak, Strawberry Crater, and nearby basaltic vents. Major elements are shown in oxide weight %, trace element abundances (V, Sc, Ba, Rb, Zr, Ni) are in ppm

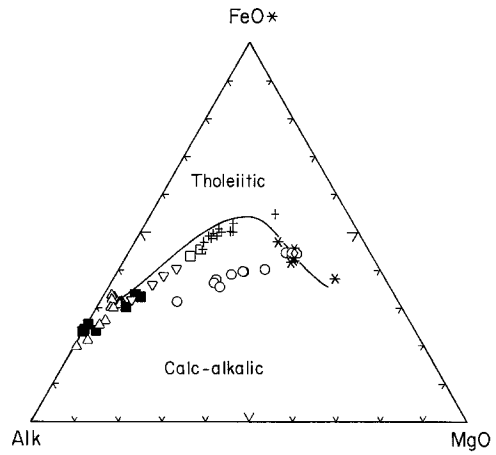

Fig. 10. AFM diagram for O'Leary Peak, Strawberry Crater and nearby vents. The line is the divisor between the tholeiitic and calc-alkaline fields of Irvine and Baragar (1971). Symbols are the same as in Fig. 9

Least-squares mixing model for Strawberry Crater

Geochemical data from Strawberry Crater also define linear major and trace element trends (Fig. 9). For all the major elements, the compositions fall along a line that is defined by the most mafic and most silicic Strawberry Crater samples, which also extrapolates to the composition of the northern dome rhyolite. The major element chemistry for Strawberry Crater samples defines a trend that is quite distinct from the O'Leary trend, but both appear to be anchored at the northern dome rhyolite composition.

With a least-squares mixing model, the major element compositions of the intermediate samples of Strawberry Crater were successfully modeled using a bimodal mixture of the most mafic Strawberry sample (80302G) and the O'Leary northern dome rhyolite. For example, the major element composition of sample 80403 can be modeled as a mixture of 52.2% 80302G and 47.8% northern dome rhyolite, and sample 80303 can be modeled as 31.3% 80302G and 68.7% Qord. The fit is excellent (Table 8, Models 7, 8).

The trace elements also vary linearly with SiO_2 (Fig. 9), although the northern dome rhyolite is not a suitable end-point for all the trace elements. The concentrations of Th, V, Sr, Sc, Y, Ce and Nd in the intermediate rocks can be successfully modeled using the northern dome rhyolite as a possible end-member, but the linear variation of La, Ba, Zr, Nb, and Rb with SiO_2 does not extrapolate to the northern dome composition. Although the northern dome rhyolite is similar to the silicic end-member in the binary mixture, the trace element chemistry indicates that the northern dome must be distinct from the actual silicic end-member (Table 8, Models 6, 7, 8).

In order to test the binary mixing model further, the most silicic and most mafic Strawberry Crater samples (80303 and 80302G, respectively) were used as end-members to determine whether the trace element abundances fit a mixing model that is based on major element chemistry. Whether or not 80303 is the true silicic end-member as opposed to an intermediate mixing product, 80303 should fall on a line between the two end-members if mixing has produced the chemical spectrum. Using a mixing ratio of 80303 and 80302G modeled to fit the major element chemistry, the trace element concentrations expected in the intermediate samples were calculated and compared to measured values. The fit is excellent for most trace elements present above detection limits (Sr, Sc, Rb,

Ba, Nb, Zr, La, V, Nd, Y, Zn, Ce and Th) (Table 8, Models 9–12) indicating that these concentrations vary linearly and suggesting that the compositions of the intermediate samples result from a binary mixing process. However, Ni and Cr concentrations do not fit the binary mixing model. The intermediate samples have Ni and Cr concentrations that are considerably lower than the modeled values (Table 8, Models 9–12). This can be attributed to minor olivine and spinel fractionation, which also accounts for the slight modeling errors in calculated MgO and SiO_2 observed for samples 72206A, 72206C, and 80403.

Phase relations and fractional crystallization

Another test of the binary mixing model is to examine the distribution of bulk compositional variations with respect to the experimentally determined phase relations appropriate for these magma types. The compositions of the units from both Strawberry Crater and the O'Leary suite project across the low-pressure thermal divide of the olivine-clinopyroxene-plagioclase-SiO_2 system (Grove and Baker 1984) (Fig. 11). Magma compositions that project within the olivine+plagioclase primary phase volume (such as the vent basalts and the xenoliths) can be driven across the thermal divide by mixing with rhyolite magma or through assimilation of crustal felsic materials, but low pressure fractional crystallization of olivine-plagioclase-clinopyroxene from such basalts will not result in compositional variations that cross the divide (Grove et al. 1982; Grove and Baker 1984).

The positions of the cotectics and thermal divide shift towards the olivine apex with increasing pressure, and thus the effects of high pressure fractional crystallization must also be considered. Some high pressure (7–10 kbar) fractional crystallization has occurred in the SFVF as a whole. Evidence includes a thermobarometric study of cumulate xenoliths by Keating and Arculus (1986), and the appearance of orthopyroxene in equilibrium with clinopyroxene at higher Mg Nos. in the cumulate assemblages than those characteristic of the phenocryst populations (Arculus et al., in preparation). However, trace element variations of the studied volcanic suites are inconsistent with formation of the O'Leary and Strawberry intermediate lavas solely by fractional crystallization at deep crustal levels. Concentrations of compatible elements such as V, Sc, Ni, Cr in the Strawberry Crater andesites are much too high for these lavas to have been produced through fractional crystallization involving olivine or clinopyroxene. Also, the major element chemistry of both the Strawberry Crater suite and the O'Leary suite cannot be modeled as fractionation of plagioclase+olivine+clinopyroxene from the basalt 72201B (O'Leary) or 80302G (Strawberry) using observed phenocryst phase compositions. AFC models yield the best results with 100% assimilation which is equivalent to binary mixing.

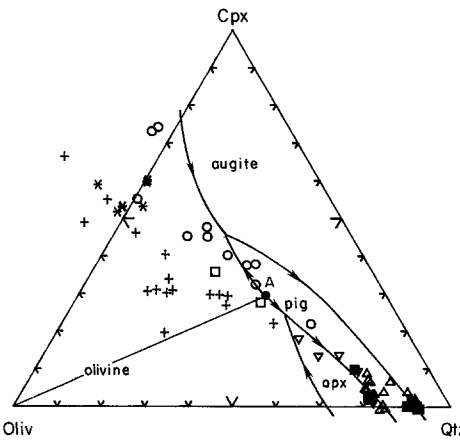

Fig. 11. Plagioclase saturated, oxygen-weighted, molar projection of the O'Leary Peak, Strawberry Crater, and basaltic vent data with the phase relations determined by Grove and Baker (1984). The *line* between the olivine vertex and point A is a low pressure thermal divide. The *points* which plot off the diagram are silica undersaturated in this projection scheme. Symbols are the same as in Fig. 9

Mixing vs comingling and assimilation

If we accept the bimodal mixing models for O'Leary Peak and for Strawberry Crater, the physical state of the end-members (solid or magmatic) at the time of mixing needs to be constrained. Either the silicic end-member is magmatic and the mafic is solid, the mafic end-member is magmatic and the silicic is solid, or both are magmatic.

In the case of the O'Leary Peak volcanics, the first possibility may be ruled out because of thermal considerations. To produce the full spectrum of intermediate rocks observed, the rhyolite would have to assimilate at least two times its weight of basalt. For example, the andesite pyroclastic deposit (which is clearly molten at the time of eruption) is compositionally equivalent to a mixture of 70% basalt and 30% rhyolite. The heat of fusion for the solid basalt (assuming the mafic rock was already at its solidus temperature) must be supplied by the latent heat of crystallization of the crystallizing phases in the rhyolite (Bowen 1928), but it would be impossible for the specific rhyolite to melt over twice its weight of basalt (a 30–70 mix) (Taylor 1980; DePaolo 1981), because the rhyolite would crystallize completely.

The second possibility suffers similar thermal constraints because the basalt would have to assimilate over three times its weight of rhyolite to produce the observed spectrum (eg. Darton Dome=77% Qord). Furthermore, if a lava similar to the northern dome represents the silicic end-member, then its magmatic character at the time of mixing is supported by the presence of mafic xenoliths within it.

Depending on the temperatures and relative proportions of two mixing magmas (basalt and rhyolite), the resultant mixture may be relatively homogeneous (a "hybrid") or may have compositional heterogeneity (e.g., banding or inclusions of basalt in a rhyolite). Based on the rapidity of thermal diffusion relative to chemical diffusion, Sparks and Marshall (1986) proposed that formation of a hybrid magma, which occurs through chemical diffusion, requires that the two mixed magmas both behave as liquids with low viscosity after thermal equilibrium is reached. When a large proportion of cooler, more viscous rhyolite magma is mixed with a basalt magma, the temperature of equilibration is relatively low and the basalt magma will tend to behave as a solid suspended in the rhyolite magma. Chemical diffusion will be inhibited and complete homogenization is unlikely. This is consistent with the observations in the O'Leary suite. The northern dome rhyolite and Darton Dome dacite contain abundant basaltic and andesitic inclusions that probably resulted from incomplete hybridization due to the high ratio of rhyolite to basalt in the mixtures. In the basaltic andesite units, the ratio of rhyolite to basalt

was much lower, resulting in homogeneous hybrid magmas such as the pyroclastic deposit and the andesitic xenoliths.

Most importantly however, textural evidence suggests that magma mixing is the most appropriate explanation for the observed chemical trends in the O'Leary and Strawberry volcanics. Several of the xenoliths show quenched rinds where they contact the host lavas (Fig. 8) and such inclusions are often interpreted as solidified globules of magma (Eichelberger 1978; Bacon 1986). The presence of oligoclase and quartz xenocrysts in the andesitic xenoliths supports the theory that the xenoliths are magmatic inclusions, because the compositions of the oligoclase xenocrysts overlap the compositions of the oligoclase phenocrysts found in the northern dome rhyolite. This suggests that the xenocrysts may originally have been phenocrysts in the rhyolite end-member that subsequently got incorporated into the hybrid mixture (the andesite xenolith).

The reverse zoning observed in the pyroxene and plagioclase phenocrysts in the O'Leary units and their xenoliths as well as in the Strawberry Crater units is also consistent with magma mixing. Although reverse zoning in plagioclase is not conclusive, as it can result from changes in P_{H_2O} (Yoder 1968; Arculus and Wills 1980), reverse zoning in pyroxenes is accepted as evidence of open system behavior (e.g., Sakuyama 1981).

Many samples contain andesine and labradorite feldspar xenocrysts (An_{33-46} and An_{59-61}) which are partially melted (sieve-cored) and have compositions that are in some cases more An-rich than the euhedral, or rounded, or groundmass feldspar populations in the same sample. These An-rich xenocrysts may have been phenocrysts in the mafic end-member, but in the case of Strawberry Crater, they are generally not as An-rich as the euhedral feldspar phenocrysts found in the end-member basalts (An_{60-69}). They may have formed in a magma that is more mafic than the one in which they are found, which would require several stages of melt mixing. They may also represent changing P_{H_2O} conditions in the magma chamber or crustal debris from assimilation. Plagioclase feldspars from crustal granulite xenoliths found in other parts of the SFVF have been analyzed and have comparable compositions (Fig. 3, Table 3, Arculus et al. in prep.).

Lead isotopic studies (Everson 1979) suggest that there is some crustal involvement in the genesis of volcanics in the SFVF as a whole, given a decrease in $^{206}Pb/^{204}Pb$ in the sequence basalt to rhyolite. Studies based on Sr isotopes in the SFVF have led some workers to conclude that there is minimal crustal contamination (Moore et al. 1974; Pushkar and Stoeser 1975), but Sr isotopes may be insensitive to crustal contamination due to the high initial Sr content of the basaltic magmas (which may buffer the contamination effects) and the low $^{87}Sr/^{86}Sr$ characteristic of lower crustal granulites in the SFVF (D. Nealey personal communication 1987). None of the studies to date has examined a cogenetic suite in detail, and it is clear that combined Sr–Nd–Pb analyses are required.

Relationship between vents and xenoliths

Based on major element and trace element data presented earlier, the relationship between the basaltic xenoliths in the O'Leary units ("xenolith basalts") and the vent basalts may generally be one of derivative and parent, respectively. The xenolith basalts are depleted in Ni and Cr, which suggests that they are not primary liquids, and may be the

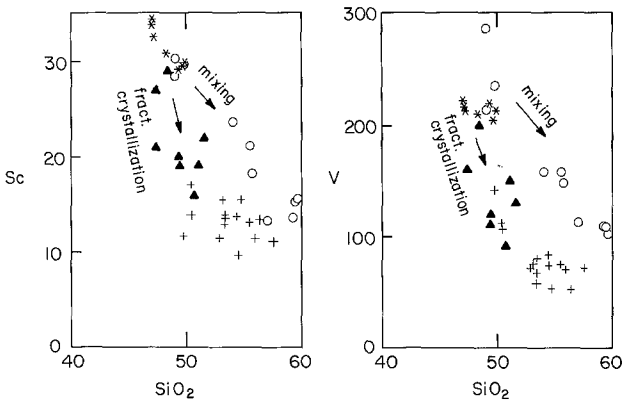

Fig. 12. This diagram shows the possible parent-derivative relationship between the O'Leary xenolith basalts (+) and the vent basalts (*). Intermediate data points between these two fields (*solid triangles*) are from USGS data (Moore and Wolfe (1987), Newhall et al. (1987), Ulrich and Bailey (1987), Wolfe et al. (1987a), Wolfe et al. (1987b)) and demonstrate that there are magmas present in the SFVF that might be representative of intermediate stages of differentiation between the more primitive vent basalts and the xenolith basalts. Also shown are Strawberry Crater samples (*open circles*)

product of fractionation of more primitive basalt. The major element chemistry is broadly consistent with derivation of the xenolithic basalts by olivine-clinopyroxene-magnetite-plagioclase fractionation from a basalt such as the most primitive Strawberry Crater sample or the vent sample 80404. The SiO_2 variation diagrams for the compatible elements Sc, V, Ni, and Cr (mineral-melt $K_D > 1$ in the crystallizing assemblage) show that an exponential decrease in these elements with SiO_2 could result from fractional crystallization of compositions similar to the Strawberry Crater or vent 80404 basalts. Samples falling between these two end-members along a possible differentiation path were not found in this study, but unpublished data from the U.S.G.S. (E. Wolfe, G. Ulrich, R. Moore personal communication) include several basalt types with Sc and V concentrations that lie along such a fractional crystallization trend (Fig. 12). The variation in Ce/Y between the Strawberry Crater basalts and the O'Leary xenolith basalts indicates that these two basalt types are not directly related by simple fractional crystallization. However, the O'Leary xenolith basalts may be derivative of other vent basalts (eg. 73105A Ce/Y = 2.8).

Origin of the silicic melts

In summary of the preceeding geochemical data, compositional variations do not indicate that the O'Leary dome rhyolite formed by fractional crystallization of any of the observed lavas. Rather, the O'Leary rhyolite is suggested to be a crustal melt and it has a composition that is broadly consistent with eutectic melting at about 5 kbar or slightly greater (Tuttle and Bowen 1958) (Fig. 13). The $^{87}Sr/^{86}Sr$ ratio measured for the O'Leary dome is 0.7050 (Moore et al. 1974), comparable to values measured for some crustal xenoliths from the SFVF (0.7058 for a quartz monzonite and 0.7057 for a gneiss (Pushkar and Stoeser 1975). Lead isotopic data indicate a relatively unradiogenic source for the SFVF silicic melts, with $^{206}Pb/^{204}Pb$ as low as 17.4 and $^{207}Pb/^{204}Pb$ as low as 15.5 (Everson 1979). Silicic melt generation may have occurred in the lower crust by melting of mafic to felsic granulite materials.

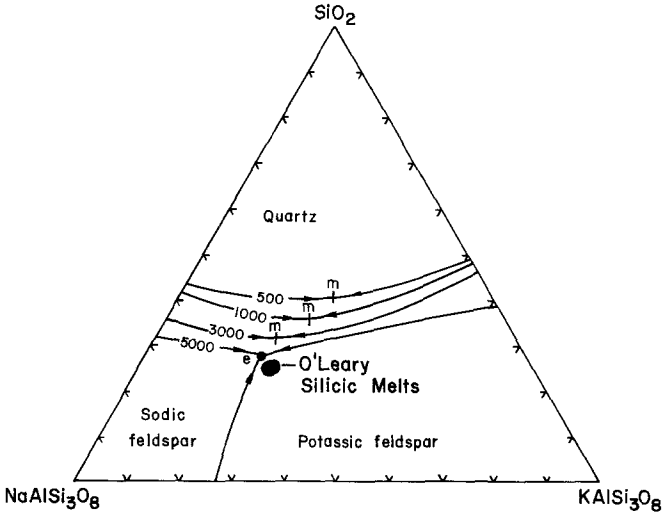

Fig. 13. Normative quartz, albite, and orthoclase content for the silicic O'Leary units shown with melting relations determined by Tuttle and Bowen (1958). The normative compositions of the silicic melts correspond to possible eutectic melting (point *e*) at about 5 kbar or slightly greater. Also shown are the 0.5, 1, 3 kbar cotectics and isobaric minima (*m*). Curves are for water-saturated liquids

Other O'Leary rhyolites and dacites, which do not fit the O'Leary binary mixing model (Qor, Qorr, Qod, Qoo), appear to define a third trend that is evident in several of the element-element diagrams, such as MnO vs MgO, Zr vs SiO_2, and Ba vs SiO_2 (Fig. 9). Based on the major and trace element geochemistry, these units do not appear to be fractionation products of the more mafic O'Leary units. Qor, Qod, and Qoo are unusual in their high Zr content (up to 580 ppm). Zr saturation in silicic peraluminous melts has been determined to be about 100 ppm, and partial melting of crustal material containing >100 ppm Zr will produce melts that are buffered at constant low (<100 ppm) Zr concentrations (Watson 1982). Thus the high Zr concentrations, well above zircon saturation levels, indicate that these melts cannot be the results of only partial melting. While excess zircon may have accumulated during crystal fractionation, there is no chemical evidence that these melts are the products of fractional crystallization of any of the sampled O'Leary lavas or vent basalts. In addition, accumulated euhedral, magmatic zircons are not abundant in thin section. These melts may have contained zircon-rich crustal debris from incomplete crustal melting or wallrock assimilation. The presence of partially melted, disequilibrium feldspars provides evidence that these melts do contain material that is not completely assimilated. The high Zr content of these flows follows a trend toward the high Zr (up to 900 ppm) observed in the peralkaline Doyle Saddle rhyolite in the San Francisco Mountain (Arculus et al. in preparation), which may represent another silicic component involved in the genesis of some the O'Leary lavas.

Conclusions

In light of the geochemistry and petrography, mixing is considered to be the most likely process involved in the petrogenesis of the intermediate lavas of O'Leary Peak and Strawberry Crater. The presence of reversely zoned phenocrysts, xenocrysts with reaction rims, magmatic inclusions with chilled margins, and the linear major and trace element variations all support the magma mixing models. Least squares mass balance calculations indicate that binary mixing can account for the observed intermediate lava compositions and that fractional crystallization processes were not significant in the generation of the intermediate melts. Fractional crystallization of a primitive basalt may have been important in the formation of the O'Leary end-member basalt.

A possible scenario is that mantle-derived basalts, emplaced in the lower crust, cause crustal melting and produce rhyolitic melts that may mix with the mantle derived basalts or with differentiated basalts that form when basalts pond and undergo fractional crystallization. Thus, the intermediate volcanic rocks of O'Leary Peak and Strawberry Crater are the products of crustal recycling, the result of basalt-driven crustal melting and the subsequent mixing of the silicic melts with mantle basalts and derivative magmas. In this particular instance, it appears that the mixing model of Eichelberger (1975, 1978) is supported by geochemical, petrographic, and preliminary isotopic data. Remaining questions as to the petrogenesis of the O'Leary units that do not fit the mixing model, as well as the origin of the end-member melts, may be answered through ongoing isotopic studies.

Acknowledgements. This research was supported in part by grant No. EAR-85-18060 from the National Science Foundation and in part by GSA grant No. 3543-86, a Sigma Xi Grant-in-Aid of Research, and the University of Michigan Turner fund. The University of Michigan electron microprobe used in this work was acquired with NSF grant No. EAR-82-12764. This project was initiated as a result of ongoing investigations in the SFVF in collaboration with Ed Wolfe, George Ulrich and Dick Moore of the U.S.G.S. and David Gust of the University of New Hampshire. Their advice on many petrogenetic issues has been influential. The authors extend their appreciation to Laura S. Kong for her assistance in the field. We also appreciate the comments of Eric J. Essene, the assistance of Abdulkader M. Afifi, Carl Henderson, Jim Hinchcliff, Susan Fast, Lisa Donaghe, and Kevin Righter. Nancy McMillan and David Gerlach provided thorough and constructive reviews of the manuscript.

References

Allegre CJ, Minster JF (1978) Quantitative models of trace element behavior in magmatic processes. Earth Planet Sci Lett 38:1–25

Arculus RJ (1987) The significance of source versus process in the tectonic controls of magma genesis. J Volcan Geotherm Res 32:1–12

Arculus RJ, Wills KJA (1980) The petrology of plutonic blocks and inclusions from the Lesser Antilles arc. J Petrol 21:743–799

Bacon CR (1986) Magmatic inclusions in silicic and intermediate volcanic rocks. J Geophys Res 91:6091–6112

Bladh KL (1980) Rapakivi texture from the O'Leary Porphyry, Arizona (USA). Bull Volcanol 43-1:155–171

Bowen NL (1928) The evolution of the igneous rocks. Dover, New York, 334 pp

Carmichael ISE (1964) The petrology of Thingmuli, a Tertiary volcano in eastern Iceland. J Petrol 5:435–460

Christiansen RL, Lipman PW (1972) Cenozoic volcanism and plate-tectonic evolution of the western United States: II Late Cenozoic. Phil Trans R Soc London A 271:269–286

Damon PE, Shafiqullah M, Levanthal JS (1974) K–Ar chronology for the San Francisco volcanic field and rate of erosion of the Little Colorado River. In: Karlstrom TNV, Swann GA, Eastwood RL (eds) Geology of Northern Arizona, with notes on archaeology and paleoclimate; Pt I, Regional studies. Geol Soc Am Rocky Mountain Sec Mtg, Flagstaff, Ariz, pp 221–235

DePaolo DJ (1981) Trace element and isotopic effects of combined wallrock assimilation and fractional crystallization. Earth Planet Sci Lett 53:189–202

Dickinson WR, Snyder WS (1979) Geometry of subducted slabs related to San Andreas transform. J Geology 87:609–627
Eichelberger JC (1975) Origin of andesite and dacite: evidence of mixing at Glass Mountain in California and at other circum-Pacific volcanoes. Geol Soc Am Bull 86:1381–1391
Eichelberger JC (1978) Andesite volcanism and crustal evolution. Nature 275:21–27
Everson JE (1979) Regional variation in the lead isotopic characteristics of late Cenozoic basalts from the southwestern United States. Unpub PhD dissertation, Cal Inst Tech, 452 pp
Gill JB (1981) Orogenic andesites and plate tectonics. Springer, New York Berlin Heidelberg, 390 pp
Grove TL, Baker MB (1984) Phase equilibrium controls of the tholeiitic versus calc-alkaline differentiation trends. J Geophys Res 89:3253–3274
Grove TL, Gerlach DC, Sando TW (1982) Origin of calc-alkaline series lavas at Medicine Lake volcano by fractionation, assimilation, and mixing. Contrib Mineral Petrol 80:160–182
Gust DA, Arculus RJ (1986) Petrogenesis of alkalic and calcalkalic volcanic rocks of Mormon Mountain Volcanic Field, Arizona. Contrib Mineral Petrol 94:416–426
Harvey PK, Taylor DM, Hendry RD, Bancroft F (1973) An accurate fusion method for the analysis of rocks and chemically related materials by X-Ray fluorescence spectrometry. X-Ray Spectrom 2:33–44
Hildreth W (1981) Gradients in silicic magma chambers: implications for lithospheric magmatism. J Geophys Res 86:10153–10192
Huebner JS, Turnock AC (1980) The melting relations at 1 bar of pyroxenes composed largely of Ca-, Mg-, and Fe-bearing components. Am Mineral 65:225–271
Irvine TN, Baragar WRA (1971) A guide to the chemical classification of the common volcanic rocks. Can J Earth Sci 8:543–548
Keating S, Arculus RJ (1986) The assemblage opx-cpx-plag-spinel as a reliable geobarometer for igneous and metamorphic rocks. (abstract) Geol Soc Am Abstr Prog 18:652
Langmuir CH, Bender JF, Bence AE, Hanson GN (1977) Petrogenesis of basalts from the FAMOUS area: mid-Atlantic ridge. Earth Planet Sci Lett 36:133–156
Langmuir CH, Vocke RD Jr, Hanson GN (1978) A general mixing equation with applications to Icelandic basalts. Earth Planet Sci Lett 37:380–392
LeBas MJ, LeMaitre RW, Streckeisen A, Zanettin B (1986) A chemical classification of volcanic rocks based on the total alkali-silica diagram. J Petrol 27:745–750
LeMaitre RW (1981) Genmix – a generalized petrological mixing model program. Computers and Geosciences 7:229–247
Lindsley DH (1983) Pyroxene thermometry. Am Mineral 68:477–493
Lipman PW (1975) Evolution of the Platoro caldera complex and related volcanic rocks, southeastern San Juan Mountains, Colorado. US Geol Surv Prof Paper 852 128 pp
MacDonald GA (1968) Composition and origin of Hawaiian lavas. Geol Soc Am Mem 116:477–552
MacDonald GA, Katsura T (1964) Chemical composition of Hawaiian lavas. J Petrology 5:82–133
Moore RB, Ulrich GE, Wolfe EW (1974) Geology of the eastern and northern parts of the San Francisco volcanic field, Arizona. In: Karlstrom TNV, Swann GA, Eastwood RL (eds) Geology of Northern Arizona, with notes on archaeology and paleoclimate; Pt II, Area studies and field guides. Geol Soc Am Rocky Mountain Sec Mtg, Flagstaff, Ariz, pp 465–494
Moore RB, Wolfe EW (1976) Geologic map of the eastern San Francisco volcanic field, Arizona. Miscellaneous Investigation Series, US Geol Surv, Map I-953
Moore RB, Wolfe EW (1987) Geologic map of the east part of the San Francisco Volcanic Field, north-central Arizona. Miscellaneous Field Studies, US Geol Surv, Map MF-1960
Moore RB, Wolfe EW, Ulrich GE (1976) Volcanic rocks of the eastern and northern parts of the San Francisco Volcanic Field, Arizona. US Geol Surv J Res 4:549–560
Newhall CG, Ulrich GE, Wolfe EW (1987) Geologic map of the southwest part of the San Francisco Volcanic Field, north-central Arizona. Miscellaneous Field Studies, US Geol Surv, Map MF-1958
Norrish K, Chappell BW (1967) Physical methods in determinative mineralogy. J Zussman (ed) Chap 4 Academic Press, New York
Norrish K, Hutton JT (1969) An accurate X-ray spectrographic method for the analysis of a wide range of geologic samples. Geochim Cosmochim Acta 33:431–453
Pushkar P, Stoeser DB (1975) $^{87}Sr/^{86}Sr$ ratios in some volcanic rocks and some semifused inclusions of the San Francisco volcanic field. Geology 3:669–671
Quilivan WD, Byers FM Jr (1977) Chemical data and variation diagrams of igneous rocks from the Timber Mountain-Oasis Valley caldera complex, southern Nevada. US Geol Surv Open-File Rep 77–724, pp 9
Robinson HH (1913) The San Franciscan Volcanic Field, Arizona. US Geol Surv Prof Paper 76
Sakuyama M (1981) Petrological study of the Myoko and Kurohime volcanoes, Japan: crystallization sequence and evidence for magma mixing. J Petrol 22:553–583
Smiley TL (1958) The geology and dating of Sunset Crater, Flagstaff, Arizona, in New Mexico. Geol Soc 9th Field Conf, Guidebook of the Black Mesa Basin 186–190 pp
Sparks RSJ, Marshall LA (1986) Thermal and mechanical constraints on mixing between mafic and silicic magmas. J Volcan Geotherm Res 29:99–124
Spencer KJ, Lindsley DH (1981) A solution model for coexisting iron-titanium oxides. Am Mineral 66:1189–1201
Stoeser DB (1974) Xenoliths of the San Francisco volcanic field, northern Arizona. In: Karlstrom TNV, Swann GA, Eastwood RL (eds) Geology of Northern Arizona, with notes on archaeology and paleoclimate; Pt II, Area studies and field guides. Geol Soc Am Rocky Mountain Sec Mtg, Flagstaff, Ariz, pp 530–545
Stormer JC Jr (1983) The effects of recalculation on estimates of temperature and oxygen fugacity from analyses of multicomponent iron-titanium oxides. Am Mineral 68:586–594
Tanaka KL, Shoemaker EM, Ulrich GE, Wolfe EW (1986) Migration of volcanism in the San Francisco volcanic field, Arizona. Geol Soc Am Bull 97:129–141
Taylor HP Jr (1980) The effects of assimilation of country rocks by magmas on 18O/16O and 87Sr/86Sr systematics in igneous rocks. Earth Planet Sci Lett 47:243–254
Tuttle OF, Bowen NL (1958) Origin of granite in the light of experimental studies in the system $NaAlSi_3O_8-KAlSi_3O_8-SiO_2-H_2O$. Geol Soc Am Mem 74
Ulrich GE, Bailey NG (1987) Geologic map of the SP Mountain part of the San Francisco Volcanic Field, north-central Arizona. Miscellaneous Field Studies, US Geol Surv, Map MF-1956
Watson EB (1979) Zircon saturation in felsic liquids: experimental results and applications to trace element geochemistry. Contrib Mineral Petrol 70:407–419
Wenrich-Verbeek KJ (1979) The petrogenesis and trace-element geochemistry of intermediate lavas from Humphreys Peak, San Francisco Volcanic Field, Arizona. Tectonophysics 61:103–129
Wolfe EW, Ulrich GE, Newhall CG (1987) Geologic map of the northwest part of the San Francisco Volcanic Field, north-central Arizona. Miscellaneous Field Studies, US Geol Surv, Map MF-1957
Wolfe EW, Ulrich GE, Holm RF, Moore RB, Newhall CG (1987) Geologic map of the central part of the San Francisco Volcanic Field, north-central Arizona. Miscellaneous Field Studies, US Geol Surv, Map MF-1959
Yoder HS (1968) Experimental studies bearing on the origin of anorthosite. In: YW Isachesen (ed) Origin of anorthosite and related rocks. University of the State of New York, Albany, p 13–23

Received October 23, 1988 / Accepted April 4, 1989
Editorial responsibility: T. Grove